

3D-focusing Spectrometer for a Reaction Microscope



Christian Dornes

Fakultät für Physik und Astronomie
Ruprecht-Karls-Universität Heidelberg

A thesis submitted for the degree of
Diplom im Studiengang Physik

December 2011

Fakultät für Physik und Astronomie

Ruprecht-Karls-Universität Heidelberg

Diplomarbeit
im Studiengang Physik

vorgelegt von
Christian Dornes

geb. in Münster (Westf.)

Dezember 2011

3D-focusing Spectrometer for a Reaction Microscope

This diploma thesis was carried out by Christian Dornes at the
Max Planck Institute for Nuclear Physics in Heidelberg
under the supervision of
Priv. Doz. Dr. Alexander Dorn

Abstract (Engl./dt.)

3D-FOCUSING SPECTROMETER FOR A REACTION MICROSCOPE

Within this thesis, two main improvements to an existing reaction microscope setup with a magneto-optically trapped lithium target are presented. Firstly, a flexible electrostatic lensing system for spatial focusing in the ion spectrometer has been implemented and characterised, enabling future experiments with unfocused projectile beams. Secondly, a new coil design for the magneto-optical trap was realised and tested; it incorporates compensation coils and reduces both the switching time and the potentially disrupting magnetic field outside the MOT region. This improvement makes the coincident recording of ion and electron spectra possible, giving fully-differential cross sections and providing insight into the dynamics of electron correlation. Finally, measurements of multiphoton ionisation of lithium taken at the free electron laser in Hamburg at the end of 2010 will be presented.

3D-FOKUSSIERENDES SPEKTROMETER FÜR EIN REAKTIONSMIKROSKOP

Im Rahmen dieser Diplomarbeit wurde ein Reaktionsmikroskop mit einer magneto-optischen Falle für Lithium als Target in zweierlei Hinsicht verbessert. Erstens wurde ein flexibles Fokussierungssystem für das Ionenspektrometer durch eines elektrostatischen Linsensystems realisiert und vermessen. Dies ermöglicht in Zukunft Experimente mit unfokussierten Projekttilstrahlen. Zweitens wurde ein neues Spulendesign für die magneto-optischen Falle gebaut und getestet; es beinhaltet Kompensationsspulen und verringert sowohl die Schaltzeit als auch die Stärke des potentiell störenden Magnetfelds außerhalb des Fallenbereichs. Diese Verbesserung ermöglicht die koinzidente Aufzeichnung von Ionen- und Elektronenspektren und damit die Messung von vollständig differentiellen Wirkungsquerschnitten. Diese geben Einsicht in die Dynamik der Elektronenkorrelation. Zum Abschluß werden Ergebnisse zur Multiphotonenionisation von Lithium präsentiert, die Ende 2010 am Freie-Elektronen-Laser in Hamburg gemessen wurden.

Acknowledgements

I would like to acknowledge the support I received during my thesis, especially from my group colleagues Dipl.-Phys. Michael Schuricke, PhD Gopisankararao Veeravalli and my supervisor Priv.-Doz. Dr. Alexander Dorn.

Contents

1	Introduction	1
2	Laser cooling and trapping	5
2.1	The scattering force	5
2.2	Doppler cooling	7
2.3	Peculiarities of lithium	10
2.4	Zeeman slower	11
2.5	Magneto-optical trap	13
3	Experimental setup	15
3.1	Spectrometer	15
3.2	Detectors	19
3.3	Momentum reconstruction	21
3.3.1	Ions	22
3.3.2	Electrons	23
3.4	Projectiles	25
3.4.1	UV laser	25
3.4.2	Electron gun	26
3.4.3	Free electron laser	27
3.5	Target preparation	29
3.5.1	New oven and Zeeman slower	29
3.5.2	Laser system	30
3.5.3	MOT-field generation and switching	32

CONTENTS

4	Designing the focusing lens	35
4.1	Introduction to electrostatic lenses	36
4.2	Identifying constraints and performance parameters	39
4.2.1	Pattern for testing TOF focus	40
4.2.2	Pattern for testing spatial focusing on the X- and Y-axis	42
4.2.3	Pattern for testing focal plane curvature and image shape	46
4.3	The resulting design	47
5	Measurements	49
5.1	Testing the spatial focusing	49
5.1.1	Comparison to Monte Carlo simulations	53
5.2	Retaining TOF-focusing	58
5.3	Characterisation of the new MOT coils	58
6	Results from FLASH 2010	63
6.1	Introduction to photo double ionisation	63
6.2	Multiphoton ionisation	64
6.3	Preliminary results for sequential double ionisation	65
6.3.1	A look a single ionisation	68
6.4	Comparison with theory	69
7	Conclusion and outlook	73
	References	77

1

Introduction

Collision experiments that involve an electron or a photon projectile on an atom, ion, molecule, or cluster target have received an increased interest in recent years. Much of this success can be attributed to advances in experimental techniques. Many-particle imaging spectrometers, such as reaction microscopes, have been developed and refined, for example by laser cooling and trapping the atomic target. Another improvement are novel light sources: in lasers, there are now higher intensities, shorter pulses, a wider choice of wavelength and often finer control of the pulse shape available than ever before. Technology that used to be restricted to only a few specialised labs in the world is now often commercially available. At the same time, the intensity and photon energy frontiers are being advanced in large facilities using *free-electron lasers* such as the *FLASH* in Hamburg, the *LCLS* in Stanford, *SPring-8* in Japan, or the *European XFEL*, which is currently under construction.

The improvements in both fields opened the way to explore new regimes of light-matter interaction. A prominent example for this is the elucidation of the mechanism for non-sequential double ionisation in the near-infrared (NIR). Here, the combination of state-of-the-art laser technology with dedicated reaction microscopes identified laser-driven recollisions of the first ionised electron as the driving force for double ionisation in the NIR regime [1, 2, 3].

The short wavelengths and high intensities now available at free electron lasers give rise to different mechanisms in few-photon few-electron reactions. In contrast to intense NIR radiation, even intensities as high as 10^{15} W/cm^2 constitute only a tiny

1. INTRODUCTION

electric laser field in the vacuum ultraviolet. Therefore, non-sequential processes are mediated primarily through electron correlation, offering a unique possibility to study electron-electron correlation in a clean, ‘field-free’ environment [4, 5]. The understanding of these basic processes is of utmost importance, as they always occur whenever intense VUV radiation meets matter. The ultimate goal of recent ‘advanced reaction microscopes’ like the CAMP apparatus [6], namely the imaging of bio-molecules at free electron lasers, requires a good understanding of the underlying interactions.

The many-particle imaging spectrometer apparatus used for this work is a so-called MOT reaction microscope (MOTREMI). It combines the properties of a reaction microscope, given by the potential to record ion-electron coincidences over a large solid angle of up to 4π , with the ultra-cold temperatures commonly achieved in magneto-optical traps. The ultra-cold target permits an excellent momentum resolution for the recoil ions. Currently, 0.05 a.u. have been achieved, limited by imperfections in the REMI spectrometer. Considering target temperature of about $500\text{ }\mu\text{K}$ alone, values on the order of less than 0.01 a.u. are feasible, which is a big advantage over ‘traditional’ REMI setups, where the target is provided by a supersonic jet ($T \approx 1\text{ K}$). MOTREMI also allow different atomic targets compared to gas jet REMIs, which are mostly restricted to noble gases or have to operate with seeded jets.

Here, lithium was chosen as target, which strikes a good balance between simplicity and complexity. It is the simplest atom with electrons in more than one shell in the ground state and has a hydrogen-like spectrum. At the same time, it is still relatively simple to treat theoretically, with its helium-like core and the loosely bound valence electron. The three electrons present already enable many complex processes, such as different mechanisms of double and triple ionisation. Lithium is therefore a good testing ground for theoretical models seeking to explain the features of these phenomena.

This thesis was focused on improving the experimental setup in order to enable further studies on electron impact and photo ionisation of atomic lithium. In Chapter 2, the reader is introduced to the basic principles of laser cooling and trapping, before the experimental setup is described in Chapter 3. The main part of this work, the design of an electrostatic focusing lens for the ion part of the REMI spectrometer, is presented in Chapter 4. The purpose of the focusing is to gain recoil ion momentum resolution

when operating with relatively large reaction volumes. Finally, new coils for the MOT were built and characterised, greatly reducing the decay time of the magnetic field after the electric current has been switched off. Fast switching is of great importance when measuring electrons, since they are easily disturbed by residual magnetic fields. By reducing the waiting time between switch-off and data acquisition, the MOT can be operated in a more efficient manner, yielding both a denser target and a higher duty cycle. This is a necessity for the angular distribution and particle correlation measurements, which require large statistics and are often limited by the amount of data available. Chapter 5 presents characterisation measurements of the focusing lens and the new MOT coils. Finally, data taken during a beamtime campaign at FLASH will be presented and compared to new theoretical calculations in Chapter 6.

1. INTRODUCTION

2

Laser cooling and trapping

It has long been known and experimentally confirmed [7] that atoms receive a recoil momentum when absorbing a photon. However, it was the advent of tunable lasers that sparked new experimental and subsequently theoretical interest in the possibility of using light to generate well-controlled forces on neutral atoms. This development started in the late 1970s with the cooling of electromagnetically trapped ions [8, 9] as well as proof-of-concept deflection experiments [10], and accelerated around the mid-1980s. Seminal publications include the first Zeeman slower [11], the first realisation of an optical molasses [12, 13], and the magneto-optical trap [14]. Since then, many sophisticated schemes have been developed, exploiting different aspects of the interaction between atoms and light. In 1997, the Nobel Prize in Physics was awarded to Steven Chu, Claude Cohen-Tannoudji and William D. Phillips for their achievements in laser trapping and cooling, highlighting the rapid progress during the preceding decade. Another pioneer in the field, Harold Metcalf, has published a comprehensive book on the subject in 1999 (Metcalf and Van der Straten [15]), which will serve as the main reference for this chapter.

2.1 The scattering force

As mentioned above, cooling atoms by laser light can be achieved in several ways based on different principles. The most straightforward method which is often taken as synonymous with the term “laser cooling” is based on the recoil momentum that an atom gains when absorbing a resonant laser photon. In an ideal two-level system, the

2. LASER COOLING AND TRAPPING

excited atom will then decay down to the ground state again, according to the lifetime of the excited state. The outgoing photon will be emitted in a random direction. The recoil momenta from the spontaneous decays will therefore cancel when averaging over many such cycles, whereas the momenta transferred to the atom by absorbing the identical laser photons will sum up. The result is a net force on the atom in the direction of the laser beam. This force is called the *scattering force*:

$$\vec{F}_{\text{scatt}} = (\text{photon momentum} \times \text{scattering rate}) = \hbar \vec{k} \cdot \gamma_{\text{scatt}} \quad (2.1)$$

To be absorbed with a sufficient probability, the energy of the laser photon has to be close to an allowed transition line of the atom. In the usual two-level atom model, the scattering rate depends on the detuning of the laser frequency from the atomic resonance ($\delta = \omega_l - \omega_0$) as well as the intensity of the light. In a steady-state situation, where spontaneous emission and absorption are in equilibrium, the scattering rate must equal the rate of decay:

$$\gamma_{\text{scatt}} = \gamma \rho_{ee} = 2\pi\Gamma\rho_{ee} \quad (2.2)$$

Here, ρ_{ee} denotes the population of the excited state and Γ is the natural linewidth corresponding to its lifetime, i.e. $\gamma = 1/\tau$. Metcalf and Van der Straten [15] find an expression for the excited state population by solving the stationary optical Bloch equations:

$$\rho_{ee} = \frac{s}{2(1+s)} = \frac{s_0/2}{1+s_0+(2\delta/\gamma)^2} \quad (2.3)$$

with the saturation parameter

$$s = \frac{|\Omega|^2}{2|\gamma/2 - id|^2} = \frac{|\Omega|^2/2}{\delta^2 + \gamma^2/4} = \frac{s_0}{1 + (2\delta/\gamma)^2} \quad (2.4)$$

and the on-resonance saturation parameter

$$s_0 = 2|\Omega|^2/\gamma^2 = I/I_{\text{sat}} \quad (2.5)$$

where I is the intensity of the light. The *saturation intensity* is given by $I_{\text{sat}} = \pi\hbar c/3\lambda^3\tau$. For the D2-line of lithium with $\tau \approx 27$ ns and $\lambda \approx 671$ nm, which is used in the experiment, the saturation intensity is about 2.5 mW/cm², a typical value for atomic

transitions. The parameter δ is the *detuning* of the laser frequency from the atomic resonance; Ω is the *Rabi frequency*, a semi-classical quantity describing the coupling between the atomic dipole moment and the laser field. It can be interpreted as the frequency with which the atomic population oscillates between ground and excited state (*Rabi oscillations*), also described by the optical Bloch equations. Plugging these results back into the expression for the scattering force yields the Lorentzian

$$\vec{F}_{\text{scatt}} = \hbar \vec{k} \cdot \frac{\gamma}{2} \cdot \frac{s_0}{1 + s_0 + (2\delta/\gamma)^2}. \quad (2.6)$$

For high intensities, this expression converges to the maximum force $F_{\text{max}} = \hbar k \gamma / 2$. More photons can produce faster absorption rates, but stimulated emission grows equally. The momentum transfer in the latter is exactly opposite to what it is in absorption, making the sum zero. The atoms can spend at most half of the time in the excited state on average, limiting the rate of spontaneous decay and thereby the scattering force. For the D2-line, this corresponds to a scattering rate of 1.85×10^7 photons per second. The resulting force acting on the mass of ${}^7\text{Li}$ leads to an acceleration of $1.58 \times 10^6 \text{ m/s}^2$ or 160 000 g. Figure 2.1 shows that this maximum force is reached to within a few percent for intensities higher than one hundred times the saturation intensity. Increasing the laser output after this point only causes more absorption in the wings of the profile, i.e. for higher detunings. This effect is known as *power broadening* [16].

2.2 Doppler cooling

So far, equation (2.6) is valid for an atom at rest with respect to the laboratory (laser) frame. When there is a relative motion, the Doppler effect will shift the laser frequency seen by the atom by $\omega_D = -\vec{k} \cdot \vec{v}$. It acts like an additional detuning term:

$$\delta(v) = \delta(0) + \omega_D = \omega_l - \omega_0 - \vec{k} \cdot \vec{v} \quad (2.7)$$

Plugging the velocity-dependent detuning back into equation (2.6) gives a velocity-dependent force on the atoms, opening up a possibility of laser cooling. If a laser is slightly red-detuned with respect to the resonance, atoms moving against the direction

2. LASER COOLING AND TRAPPING

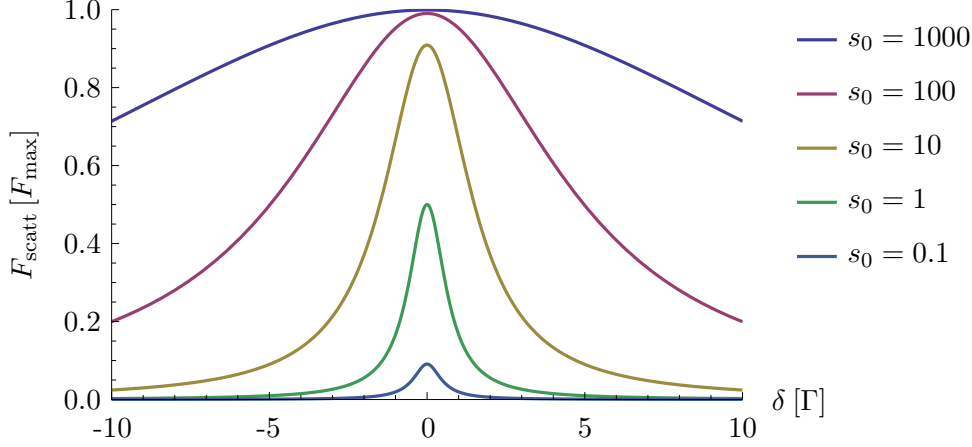


Figure 2.1: The scattering force in units of F_{\max} is shown as a function of the detuning for different saturation parameters. For low intensities, the linewidth approaches the natural linewidth Γ and the force is still relatively low. At $s_0 = 1$, the force passes half the maximum value and power broadening becomes visible. The linewidth scales with $\sqrt{1 + s_0}$.

of the laser beam will see the light blue-shifted back towards the centre of the absorption line, increasing the scattering rate and exerting more force. After adding a second counter-propagating laser beam of the same frequency, the two forces will be balanced for an atom at rest. A moving atom on the other hand will experience a net force that is slowing it down. The sum of the two beams' forces gives the expression for the total force:

$$F = F^+ + F^- = \hbar \vec{k} \cdot \frac{\gamma}{2} \cdot \frac{s_0}{1 + s_0 + (2\delta - \vec{k}\vec{v}/\gamma)^2} - \hbar \vec{k} \cdot \frac{\gamma}{2} \cdot \frac{s_0}{1 + s_0 + (2\delta + \vec{k}\vec{v}/\gamma)^2} \quad (2.8)$$

Three linearly independent, preferably orthogonal, pairs of such counter-propagating beams will provide complete translational cooling. This configuration is called an *optical molasses* (Chu et al. [12]). Figure 2.2 plots the cooling force along one of the axes, as given by equation (2.8), as a function of the velocity. The detuning was chosen as $\delta = -\gamma$, i.e. one linewidth red-detuned, and the saturation as $s_0 = 2$, following Metcalf and Van der Straten [15, p. 88]. With these parameters, the force has a nearly constant slope around $v = 0$ for $v \lesssim \gamma/k$. At this point, the Doppler shift is as big as the natural linewidth of the transition. The speed γ/k is therefore characteristic for the optical

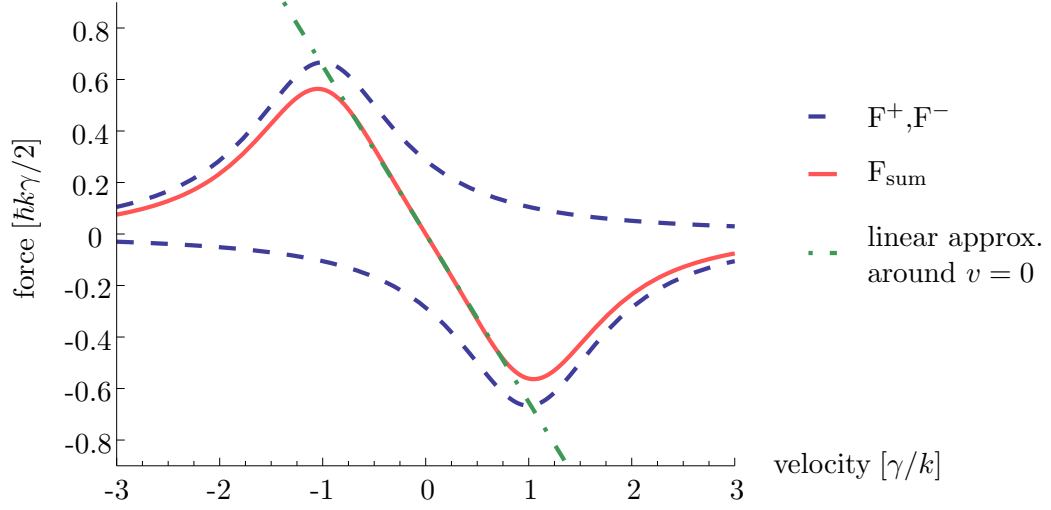


Figure 2.2: The position-dependent force in a 1D optical molasses. In blue, the contributions of the two counter-propagating beams are plotted, while the red curve shows the sum of the two forces.

molasses and also known as the *capture velocity*.

It has to be noted that equation (2.8) is not valid any more at very low velocities and forces, as it describes the time-averaged force; ultimately, when the momentum of the atom approaches the momentum of a photon from the cooling laser beam, the stochastic nature of absorption and emission becomes important. The trajectory of the atom can be described as a random walk in momentum space, caused by spontaneous emission, superimposed with velocity-dependent absorption probabilities for the laser photons, leading to another random walk process with variable weights. From these considerations, a lower limit on the temperature that can be reached by Doppler cooling can be calculated. Metcalf and Van der Straten [15] derive the following expression:

$$k_{\text{B}}T = \frac{\hbar\Gamma}{4} \left(\frac{\Gamma}{2\delta} + \frac{2\delta}{\Gamma} \right) \quad (2.9)$$

It follows that for a detuning of $\delta = -\Gamma/2$, a minimum temperature is reached:

$$T_{\text{Doppler}} = \frac{\hbar\Gamma}{2k_{\text{B}}} \quad (2.10)$$

For ^7Li with $\Gamma = 5.87 \text{ MHz}$, the Doppler-limited temperature is $T_{\text{Doppler}}(^7\text{Li}) \approx 142 \mu\text{K}$.

2.3 Peculiarities of lithium

Lithium is the the third element of the periodic table and the lightest of the alkali metals. According to modern cosmology, it was already produced during the primordial nucleosynthesis shortly after the Big Bang. It has a nuclear charge of $Z = 3$ and therefore contains an electron in the open L -shell in the neutral ground state. The isotope ${}^7\text{Li}$ is used in our magneto-optical trap; table 2.1 presents its main nuclear and atomic properties:

property	symbol	value [ref.]
proton number	Z	3
mass number	$A = Z + N$	7
relative atomic mass	m	7.016 004 55(8) amu [17]
nuclear spin / parity	J^π	$3/2^-$ [18]
1 st ionisation potential	IP_{Li}	5.391 719 eV [19]
2 nd ionisation potential	IP_{Li^+}	75.6400 eV [19]
3 rd ionisation potential	$\text{IP}_{\text{Li}^{2+}}$	122.45429 eV [19]

Table 2.1: Basic nuclear and atomic properties of ${}^7\text{Li}$.

The spectroscopic properties of lithium make Doppler cooling more complicated than in the case of an ideal two-level atom. In analogy to earlier experiments using other alkalies like sodium [14] or rubidium, the $|2^2S_{1/2}\rangle - |2^2P_{3/2}\rangle$ transition is used as the cooling transition because it is the strongest line. The difficulty with lithium is that the hyperfine splitting (HFS) of the excited $2^2P_{3/2}$ state is of the same magnitude as its natural linewidth: Figure 2.3 shows that four hyperfine sub-levels all lie within 18.33 MHz while the natural linewidth, as derived from the lifetime of 27.10 ns, is 5.87 MHz.

This overlap causes the atoms to not stay in the closed cooling cycle between the $|2^2S_{1/2}, F = 2\rangle$ and $|2^2S_{3/2}, F = 3\rangle$ states, but sometimes populate another level in the upper state and then fall down to the other hyperfine level of the ground state, $|2^2S_{1/2}, F = 1\rangle$. Due to the large hyperfine splitting of the ground state of about 800 MHz, this level cannot be re-excited by the cooling laser which has a spectral width of less than 2 MHz. The ‘wrong’ ground state becomes a so-called *dark state*; the cooling cycle is broken. To alleviate this problem, another laser of similar power as the cooling laser is needed. As shown in figure 2.3, this *repumper laser* can drive the former dark state in its own loop.

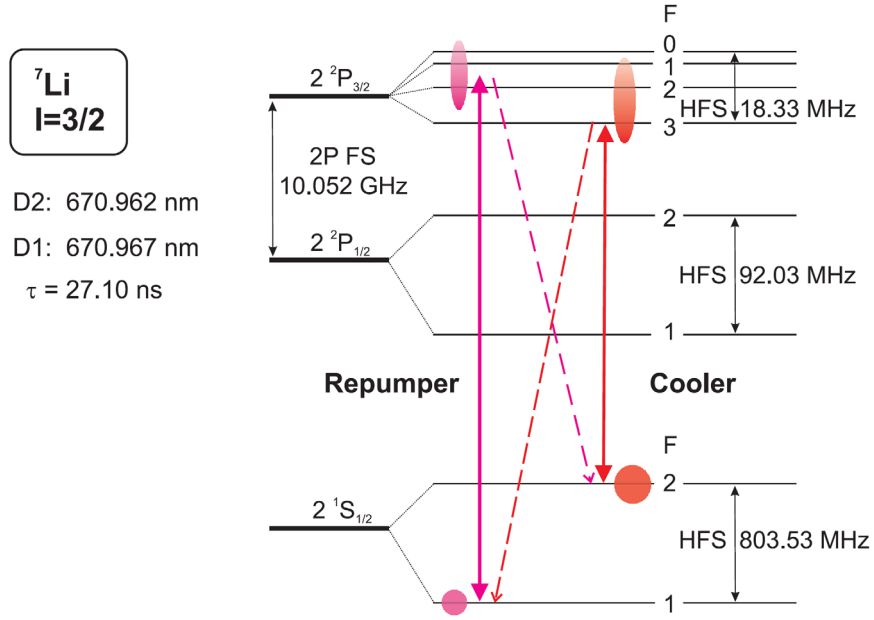


Figure 2.3: The overlapping hyperfine splitting of the $|2^2P_{3/2}\rangle$ level in ^7Li makes a strong repumper laser necessary. The solid transition lines show the two ‘closed’ cooling transitions, while the dashed lines are the additional transitions that occur due to the overlap of the hyperfine levels of the excited state. Diagram courtesy of Steinmann [20]

It is worth mentioning that the lithium used in our oven is not pure ^7Li , but a mixture of ^6Li and ^7Li , corresponding to the natural isotope abundances. When the MOT is used, we do of course not see any ^6Li in the time-of-flight spectra—it cannot be trapped with the same laser frequencies as ^7Li because of its slightly different energy levels. In contrast, when using the hot oven beam directly as a test target for the electron gun, two peaks can be seen in the time-of-flight spectra, corresponding to the masses of the two isotopes. The relative peak heights from a measurement with the pulsed electron gun operating at an electron energy of 1000 eV indicate a ratio of about 1:12, corresponding well to the values found in literature ($^6\text{Li} \approx 7.5\%$, $^7\text{Li} \approx 92.5\%$ [21]).

2.4 Zeeman slower

The purpose of this apparatus is to slow down a fast atomic beam, for example from an oven. It combines the velocity-dependent scattering force with a position-dependent magnetic field to generate a slowing force over a longer distance. Doppler cooling alone

2. LASER COOLING AND TRAPPING

only works as long as the Doppler shift is within a few times of the natural linewidth of the cooling transition. Atoms that are too fast or too slow are far from resonance, leading to a scattering rate that is too low to have a noticeable effect. The effective frequency region depends on the intensity of the laser due to power broadening (see figure 2.1). The estimated value for our experiment with 15 mW of laser power in a Gaussian MOT beam of 20 mm diameter is about two linewidths or 12 MHz, which only corresponds to a velocity difference of 8 m/s. This not enough to slow down the vast majority of faster atoms from a lithium oven beam. By using a varying magnetic field, they can be kept in resonance with the counter-propagating slowing laser much longer. The condition to cancel the Doppler shift by the Zeeman shift is given by:

$$\omega_0 + \frac{\mu_B B(z)}{\hbar} = \omega + \vec{k}\vec{v} \quad (2.11)$$

If the atoms are kept in exactly in resonance, they will be decelerated by a constant force, neglecting variations that arise from the fluctuations in the number of photons scattered per unit time. With an initial velocity v_0 and deceleration a , the total stopping distance is $L_0 = v_0^2/2a$. This leads to a position-dependent velocity of [22]

$$v(z) = v_0 \sqrt{1 - \frac{z}{L_0}}. \quad (2.12)$$

With the linear Zeeman effect, the magnetic field to compensate for this change in Doppler shift is then given by

$$B(z) = B_0 \sqrt{1 - \frac{z}{L_0}} + B_{\text{offset}}. \quad (2.13)$$

For a thermal beam with a continuous velocity distribution, the resonance condition cannot be maintained for all velocities. The best that can be done is keeping a certain velocity class of atoms on resonance over the complete slower length as they decelerate, bringing their longitudinal momentum down to the desired low value. Too close to zero is not desirable since the transverse momentum of the initially thermal atoms is not changed. Most of the atoms will therefore hit the walls of the Zeeman slower as they are decelerated; this property makes it important to keep the total distance between the oven and the trapping area short, ensuring a suitable flux.

2.5 Magneto-optical trap

An optical molasses with its velocity-dependent force can only achieve trapping in momentum space. In the magneto-optical trap, this principle is combined with a position-dependent magnetic field to generate a position-dependent force. This allows confining the cold atoms in a small region in space, providing a much denser target than the molasses alone. To illustrate how the MOT works, it is instructive to consider the one-dimensional case shown in figure 2.4.

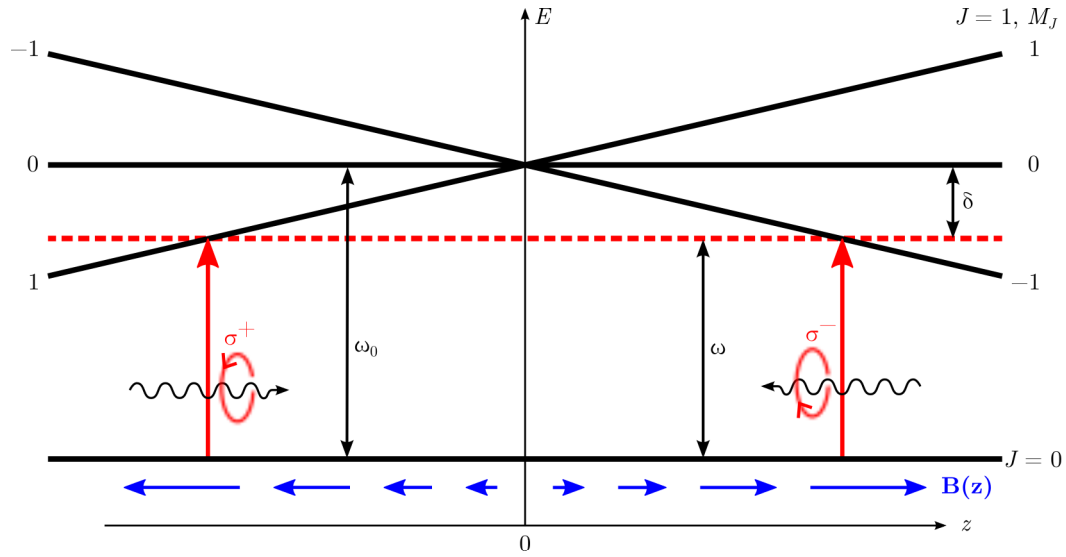


Figure 2.4: The mechanism of a magneto-optical trap for an atom with a $J = 0$ to $J = 1$ transition. The laser frequency ω is red-detuned by δ against the atomic resonance ω_0 . The Zeeman shifts have been exaggerated for illustrational purposes. Two counter-propagating circularly-polarised beams provide a restoring force that drives the atom towards the zero-point of the magnetic field. Further from the centre, the velocity needed to be in resonance with the detuned laser decreases due to the increasing Zeeman shift. Eventually, an atom at rest will be in resonance; this distance is referred to as the *capture radius* of the MOT.

Here, the angular momenta of the atomic states have to be included to account for magnetic effects. Let the ground state be $|g, J = 0\rangle$ and the excited state $|e, J = 1\rangle$; two of the three sublevels of the excited state ($m_J = \pm 1$) will experience a Zeeman shift of their energies when placed in a magnetic field, detuning them from the unperturbed resonance. When a magnetic field with constant gradient of the form $B(z) = \mu_B/\hbar \cdot \beta \cdot z$ is used, the detuning varies linearly with the position of the atom

2. LASER COOLING AND TRAPPING

along z . Including this effect yields:

$$\delta_{\text{MOT}}(v, z) = \delta - kv \pm \frac{\mu_B}{\hbar} \beta \cdot z \quad (2.14)$$

Consider now an atom displaced from the centre of the trap in positive z direction: The $M_J = -1$ transition moves closer to the red-detuned laser frequency, while the $M_J = +1$ transition moves even further away. To exploit this effect for laser cooling, circularly polarised laser beams can be used. Photons with σ^- polarisation excite the $M_J = -1$ transition, so when sending such a beam in from the right side as in figure 2.4, a scattering force that pushes the atoms back towards the centre of the trap is generated. The counter-propagating beam should be σ^+ polarised to have the same effect in the other direction. Incorporating this into the equation for the optical molasses (2.8), the scattering force becomes [22]:

$$F_{\text{MOT}}(v, z) = F^{\sigma^+}(\omega - kv - (\omega_0 + \frac{\mu_B}{\hbar} \beta \cdot z)) - F^{\sigma^-}(\omega + kv - (\omega_0 - \frac{\mu_B}{\hbar} \beta \cdot z)) \quad (2.15)$$

$$\approx -2 \frac{\partial F}{\partial \omega} kv + 2 \frac{\mu_B}{\hbar} \frac{\partial F}{\partial \omega_0} \beta z = -2 \frac{\partial F}{\partial \omega} (kv + \frac{\mu_B}{\hbar} \beta z) \quad (2.16)$$

The approximation in equation 2.15 assumes that the Zeeman and Doppler shifts are small compared to the natural linewidth ($\beta z \ll \Gamma$ and $\vec{k} \cdot \vec{v} \ll \Gamma$). The frequency $\omega_0 \pm \mu_B/\hbar \beta \cdot z$ is the resonant absorption frequency of the transition with $\Delta m_J = \pm 1$ for an atom resting at position z . The resulting force has the form $F \propto -v$, $F \propto -\beta/kz$, so there is a restoring force towards $z = 0$ and a dampening term. With the typical experimental values, the atoms undergo an over-damped simple harmonic motion [22].

In the case of a three-dimensional MOT, a pair of coils in *anti-Helmholtz configuration* is used to create a magnetic field gradient in both radial and axial direction, suited for MOT operation. Using Gauss's law for magnetism (the Maxwell equation $\text{div} \vec{B} = 0$) one can show that the gradient in any radial direction is half as strong as the one in axial direction:

$$\frac{dB_x}{dx} = \frac{dB_y}{dy} = -\frac{1}{2} \frac{dB_z}{dz} \quad (2.17)$$

3

Experimental setup

The experiment can be divided into three main parts: Firstly, a *cold lithium target* is provided by a magneto-optical trap as described in the last chapter. Secondly, a *projectile* is used to induce ionisation, producing an ion and one to three electrons, depending on the type of reaction. Finally, the *collision information* has to be extracted, which is done by a *reaction microscope* setup. Figure 3.1 shows a schematic rendering of the experiment.

Reaction microscopes are designed to make kinematically complete measurements of atomic or molecular ionisation processes. They combine COLd Target Recoil Ion Momentum Spectroscopy (COLTRIMS) with an electron spectrometer (Ullrich et al. [23, 24]). By using time and position-sensitive detectors in combination with suitable extraction fields, the momenta of all charged products created in an ionisation event can be recorded over the full solid angle.

3.1 Spectrometer

The purpose of the spectrometer is to guide the outgoing charged particles from an ionisation event to the detectors in such a way that their original momenta \vec{p} can be reconstructed. A constant electric field \mathcal{E} is applied along the spectrometer axis between two detector planes, the reaction volume being in the middle at a distance d . The positively charged particles will therefore be constantly accelerated towards one detector and the negatively charged particles towards the opposite detector. Both detectors are position and time-sensitive, giving the necessary information for the momentum recon-

3. EXPERIMENTAL SETUP

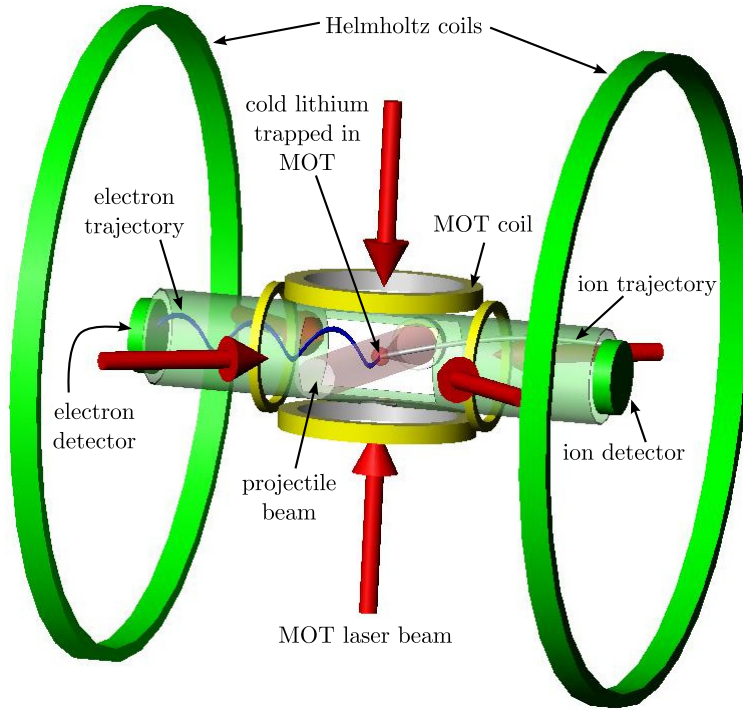


Figure 3.1: Schematic of a reaction microscope combined with a MOT target, also called MOTREMI. In the collision of the projectile beam with the cold lithium target, ions and electrons are produced, that are then guided onto position- and time-sensitive detectors by a homogeneous electric field (not shown). A pair of Helmholtz coils provides a magnetic field that confines the electron movement in transverse direction.

struction. To cover the full solid angle of 4π , \mathcal{E} must high enough to project even recoil ions with maximum transverse momentum onto the detector. This value will depend on the reactions under study.

We can easily calculate the time of flight t_0 for a particle of known mass and charge created *at rest* using Newton's equations:

$$d = \frac{1}{2} \frac{\mathcal{E}q}{m} t_0^2 \quad \Leftrightarrow \quad t_0 = \sqrt{\frac{2md}{\mathcal{E}q}} \quad (3.1)$$

If a particle is not created at rest, but with some longitudinal momentum p_{\parallel} (along the spectrometer axis), this will result in a time of flight t slightly different from t_0 . We can use this to reconstruct the original momentum p_{\parallel} :

$$d = \frac{1}{2} \frac{\mathcal{E}q}{m} t^2 + \frac{p_{\parallel}}{m} t \quad \Leftrightarrow \quad t = \sqrt{\frac{2md}{\mathcal{E}q} + \frac{p_{\parallel}^2}{\mathcal{E}^2 q^2}} \pm \frac{p_{\parallel}}{\mathcal{E}q} \quad (3.2)$$

In this expression, the '+'-sign corresponds to a particle with p_{\parallel} *away from* the detector, which increases the time of flight. Conversely, '-'-sign signifies a particle where p_{\parallel} is pointing *towards* the detector. In the experiment, the electric field strength \mathcal{E} usually lies in the range of 0.1–10 V/cm, corresponding to energies between 2.5 and 250 eV for a singly-charged ion when it hits the detector. The ion recoil momentum is on the order of atomic units, which means that the recoil energy for lithium is about $m_e/7 \text{ u} \cdot E_h \approx 2 \text{ meV}$ (where $E_h \approx 27.2 \text{ eV}$ is the Hartree energy for converting to atomic units). This big difference between the recoil energy and the energy gained due to the accelerating electric field justifies a linear approximation for t around t_0 as a function of p_{\parallel} , so equation (3.2) becomes:

$$t = t_0 \pm \frac{p_{\parallel}}{\mathcal{E}q} \quad \Leftrightarrow \quad p_{\parallel} = (t_0 - t)\mathcal{E}q \quad (3.3)$$

For the ions, it is straightforward to reconstruct the original transverse momentum \vec{p}_{\perp} from the position of impact \vec{r} on the detector measured from its centre:

$$\vec{p}_{\perp} = m\vec{v} = m\frac{\vec{r}}{t} \quad (3.4)$$

3. EXPERIMENTAL SETUP

In practice, a few refinements are made to this simple design. A good recoil momentum resolution requires very precise measurements of the time of flight and the impact position of the ion. The overlap of the MOT and the projectile beam is not exactly a point-like source, but rather has a size that can be considerably bigger (a few mm) than the spatial resolution of the detector (≈ 0.1 mm). The dimension along the spectrometer axis leads to an uncertainty in the time of flight of the order of a few hundred nanoseconds, well above the time resolution of 0.5 ns (the final ion speed at an extraction voltage of 0.1 V/cm is approximately 10 mm/ μ s). Such a big error would deny any attempt to reconstruct the small recoil momenta, but there is a simple remedy for this problem: A drift area with no electric field is added between the accelerating extraction field and the detector. The ions that happened to be produced further away from the detector will take longer to reach the end of the accelerating field, but will have reached a higher velocity when they get there. Therefore, they will catch up again with the ions that started closer to the detector. By taking the derivative of the expression for the total time of flight with respect to the deviation from the nominal starting position, we find that a drift length that is exactly twice as long as the acceleration length will leave the time of flight invariant for small deviations around the starting position. This method of cancelling the effect of the axial starting position on the time of flight in first order approximation is also called the *Wiley-McLaren configuration* [25]. The residual shift in time of flight in this *time focusing* arrangement was determined by numerical simulations. For our experiment, it is smaller than 1 ns even for targets as big as 4 mm at the smallest extraction voltages (0.1 V/cm). Therefore, p_{\parallel} can be determined very accurately. Figure 3.2 shows the geometry of the spectrometer used in the experiment, including the drift tubes at both ends.

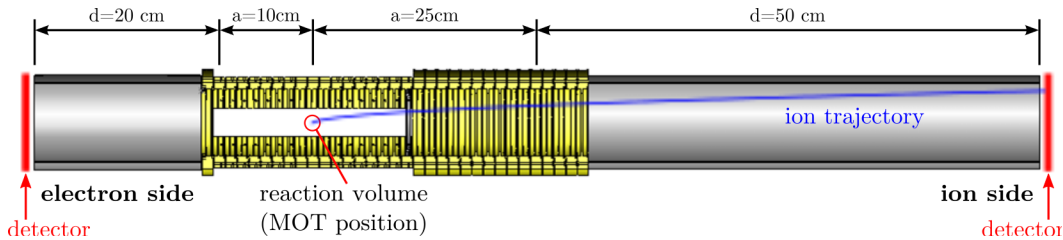


Figure 3.2: Technical drawing of the time-focusing spectrometer. The electron and ion detector positions at the end of the drift tubes are indicated.

For the radial variation in the starting position, which is parallel to the detector plane, there is no comparably simple solution. Here, the target extension leads to a loss of resolution for the detector image and thereby reduces the precision of the \vec{p}_\perp measurement. We want ions with the same momentum \vec{p} to be projected onto the same spot on the detector, regardless of their point of origin within the target, while also keeping their mutual times of flight the same. This can be realised by using an electrostatic lens, within certain limits. To determine the performance of the lens design in detail, an analytical approach is not feasible. Instead, the 3D construction files of the spectrometer were exported from a CAD program and used to perform a full numerical simulation with the *Simion* program, which will be presented in the next chapter.

The electron side of the spectrometer works in nearly the same way as the ion side. The main difference is that the electrons will attain similar momenta as the ions, but at much higher speeds due to their smaller mass. To project all the fast electrons onto the detector, it is not feasible to increase the extraction voltage; the corresponding position image for the ions would be reduced to a small spot, greatly diminishing ion recoil momentum resolution. A better solution is to apply a magnetic field along the spectrometer axis to confine the electron movement in transverse direction. When the Larmor radius is smaller than half the detector radius, the electrons will end up on the detector. In the experiment, the necessary magnetic field is created by a pair of Helmholtz coils ($r = 80$ cm). Perhaps not obvious at first sight, the full information on the electron recoil momentum can still be reconstructed from its time of flight and position on the detector, as will be shown in section 3.3.

3.2 Detectors

Both the ion and electron detector are time- and position-sensitive, realised by a stack of two *microchannel plates* (MCP) positioned in front of a *delay line anode*. An MCP is a disc made from a highly resistive material (usually lead glass) which is about 2 mm thick and has a diameter between 2–10 cm. It consists of millions of thin capillaries with a diameter of approximately $10\ \mu\text{m}$ each that have been fused together. To operate the MCP stack, a voltage of about 2000 V is applied between its front and its back side,

3. EXPERIMENTAL SETUP

making each of the hollow channels act like a photomultiplier: An ion or electron impacting on the MCP will release a few electrons from the surface, starting an avalanche due to the accelerating voltage, as shown in figure 3.3. A single MCP has a gain factor of around 10^4 . The channels of an MCP are at an angle the front surface to maximise their efficiency. When stacking two of them, it is advantageous to align the channels in a way that the angle between them is largest. Such a *chevron configuration* leads to an amplification factor of about 10^6 for the stack, yielding a much bigger electron cloud coming out of the back of the plates.

The delay-line anode that determines the position of this cloud consists of four thin copper wires that are wound around a mounting plate in pairs of two. One wire pair provides the position information along the X-axis, the other one is at an angle of 90° , covering the Y-axis. Ceramic half-tubes with grooves on the outer diameter are used to achieve even spacing of the wires as well as electrically insulating them from each other and the mounting plate. To detect the electron cloud coming out of the back of the MCP, one wire of each pair is set to a relative potential of about $+200\text{ V}$. This so-called *signal wire* will then attract the electrons, and the incoming amount of charge generates a small voltage spike that propagates towards both ends of the wire. The second wire is kept at a lower potential of about $+100\text{ V}$ and serves as a *reference wire*. As the loops of signal and reference lines are interspersed, they will pick off the same external noise, but only the signal wire has the voltage spike caused by the electrons; this allows the subtraction of the noise. Another advantage of the use of wire pairs is the decreased dispersion and dampening of the voltage peak as it travels along the signal wire; the two-wire geometry acts like a waveguide for the high radio frequencies that such a nanosecond-scale peak consists of.

For the detector on the electron side, the setup is altered slightly by introducing a third layer of wire loop pairs. These are now each at an angle of 60° with respect to the others, instead of the 90° angle between the two layers in the ion detector. For a single detector hit, this only provides redundant position information, but the advantage of the third layer is an improved multi-hit capacity due to a smaller area that is affected by dead times after a hit [26]. This allows recording all ejected electrons in measurements of double and triple ionisation. For the ions, a third layer is not needed, since only one ion is created per ionisation event. Only if a single shot of the projectile causes more than one ionisation event, there can indeed be multiple coincident hits on the ion

detector, but this can be avoided by reducing the density of the MOT or the projectile source current.

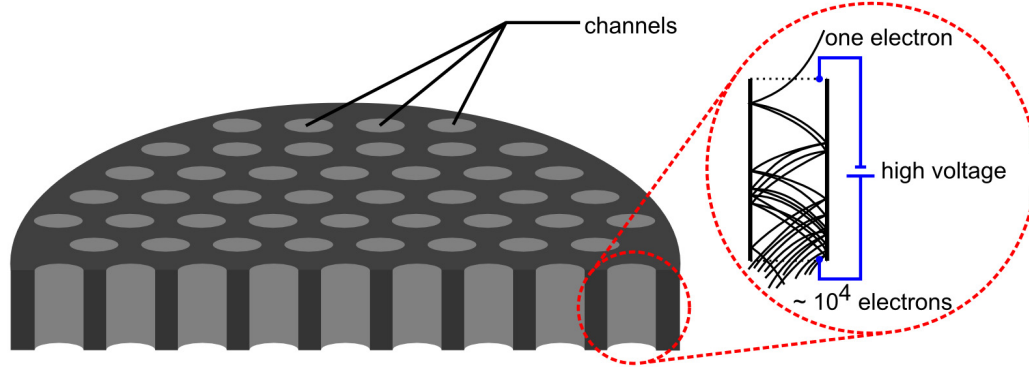


Figure 3.3: A schematic view of an MCP. One electron is entering from the top, starting an avalanche in one of the channels. In reality, the channels are not exactly perpendicular to the surface, increasing the performance. This angle also plays a role when stacking two or three MCPs in a *chevron* or *Z-configuration*.

Since the resulting signals are still only millivolt-scale peaks on top of a kilovolt-scale offset, they are coupled out capacitively. The resulting signals are then amplified by a fast amplifier and passed on to the data acquisition electronics. This is either a digitiser, writing the complete signal forms, or a chain of NIM electronics, starting with a constant fraction discriminator (CFD) and leading to a time-to-digital converter (TDC). Software or hardware, the process is conceptually very similar: The events in the different channels get an exact time stamp, and from these the number of hits, their positions, and their times of flight can be calculated.

3.3 Momentum reconstruction

The principles of recoil ion and electron momentum reconstruction were already described in section 3.1, as the spectrometer was introduced. The recoil momenta are extracted from the detector position information and the fine-structure of the time of flight; the coarse features in the ion TOF spectra correspond to particles with different ratios of q/m , for example ions from the residual gas. On the electron side, a magnetic field is used to help extracting the momentum information.

3. EXPERIMENTAL SETUP

3.3.1 Ions

Reconstructing the *longitudinal momentum* follows equations (3.1–3.3), now taking into account the drift length. An ion of mass M and charge q with longitudinal momentum p_{\parallel} is created at the interaction point; it is accelerated in a constant electric field \mathcal{E} of length a and then flies through the field-free drift region of length d with constant speed. Expressing $\mathcal{E} = U/a$ through the applied voltage and p_{\parallel} through $E_{\parallel} = p_{\parallel}^2/2m$, the equation for the time of flight is:

$$t = f \cdot \sqrt{M} \left(\frac{2a}{\sqrt{E_{\parallel}} + qU \pm \sqrt{E_{\parallel}}} + \frac{d}{\sqrt{E_{\parallel}} + qU} \right) \quad (3.5)$$

Contrary to equation (3.2), here the ‘+’-sign gives a *shorter* time of flight and corresponds to p_{\parallel} *towards* the detector. The prefactor f is introduced to use the formula directly with the desired units. For t in ns, a and d in cm, M in atomic mass units, qU and E_{\parallel} in eV it becomes:

$$f = 719.9 \cdot \frac{\text{eV}}{\text{cm}} \sqrt{\frac{\text{eV}}{\text{amu}}} \quad (3.6)$$

To solve equation (3.5) for p_{\parallel} , it is again justified to make a linear approximation in t around $p_{\parallel} = 0$:

$$\Delta t = t(E_{\parallel}) - t(E_{\parallel} = 0) \approx \left. \frac{dt}{dE_{\parallel}} \frac{dE_{\parallel}}{dp_{\parallel}} \right|_{p_{\parallel}=0} \cdot \Delta p_{\parallel} \quad (3.7)$$

The time of flight for $p_{\parallel} = 0$ is often not measured directly, but inferred from the measured spectrum by symmetry considerations. Figure 3.4 shows a typical time-of-flight spectrum for multiphoton ionisation with the centre at $p_{\parallel} = 0$ marked. Inserting equation (3.5) into (3.7), the expression for p_{\parallel} becomes (in atomic units):

$$p_{\parallel} = \left(8.042 \cdot 10^{-3} \frac{\text{cm}}{\text{eV} \cdot \text{ns}} \right) \frac{qU \cdot \Delta t}{a} \text{ a.u.} \quad (3.8)$$

The transverse momentum can be calculated by equation (3.4). In practice, the centre of the ion distribution on the detector is not exactly at the centre of the detector itself. This is caused by small deviations of the experiment from the axial symmetry, for example by the Earth’s magnetic field, the reaction volume not being precisely on-axis,

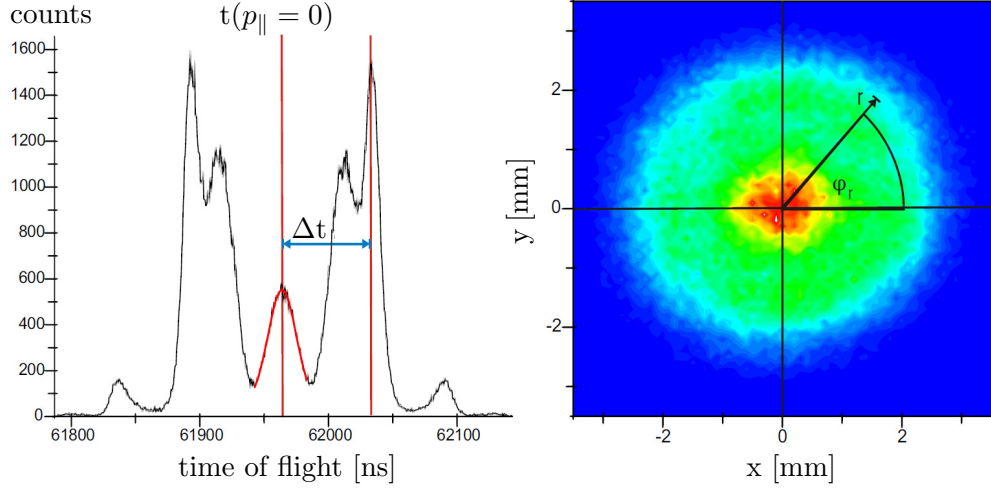


Figure 3.4: On the left, a time-of-flight spectrum for Li^+ is shown. From the time difference Δt between the centre of the distribution and a peak, the longitudinal ion recoil momentum can be calculated according to equation (3.8). On the right, the associated colour-coded position spectrum is displayed. The centre of the distribution has been determined, allowing the parametrisation in polar coordinates with the radial distance r and the azimuthal angle ϕ_r . Figure courtesy of Schuricke [27]

different stray fields from both sides of the open spectrometer, or simply tolerances. As a result, the centre is determined from the experimental data by symmetry, similarly to $t(p_{\parallel} = 0)$. With \vec{r} being the distance from this experimentally determined centre and the time of flight assumed constant, which is a good approximation ($\Delta t/t \lesssim 0.5\%$ for typical parameters), equation (3.4) becomes:

$$p_{\perp} = 11.6 \frac{\sqrt{qU \cdot M}}{\sqrt{\text{amu} \cdot \text{eV}}} \cdot \frac{\vec{r}}{2a + d} \text{ a.u.} \quad (3.9)$$

3.3.2 Electrons

For the longitudinal momenta of the electrons, equation (3.5) is equally valid since the magnetic field has no influence in this direction. However, the electrons produced in ionisation events have much higher energies than the recoil ions. The differences in time of flight for different ejection angles therefore become relatively large compared to the total time of flight. It is then no longer justified to proceed with the linear expansion as in equation (3.7). Instead, equation (3.5) has to be solved numerically for each detector hit.

3. EXPERIMENTAL SETUP

Reconstructing the transverse momenta of the electrons requires including the effect of the Helmholtz field that is guiding them onto the detector. They are following a spiral trajectory according to the Lorentz force. The radius and frequency of this motion are the Larmor radius r_e and the Larmor frequency ω , also called cyclotron frequency:

$$\omega = \frac{qB}{m_e} \qquad r_e = \frac{p_{\perp}}{qB} \qquad (3.10)$$

Figure 3.5 illustrates how the Larmor radius r_e , the radial position R_e and the cyclotron angle $\alpha = \omega \cdot t$ are connected:

$$|\sin \frac{\alpha}{2}| = \frac{R_e/2}{r_e} \qquad (3.11)$$

Using expression (3.10) for the Larmor radius allows solving equation (3.11) for the electron transverse momentum p_{\perp} . The resulting formula is:

$$p_{\perp} = \frac{qBR}{2|\sin \frac{\omega t}{2}|} \qquad (3.12)$$

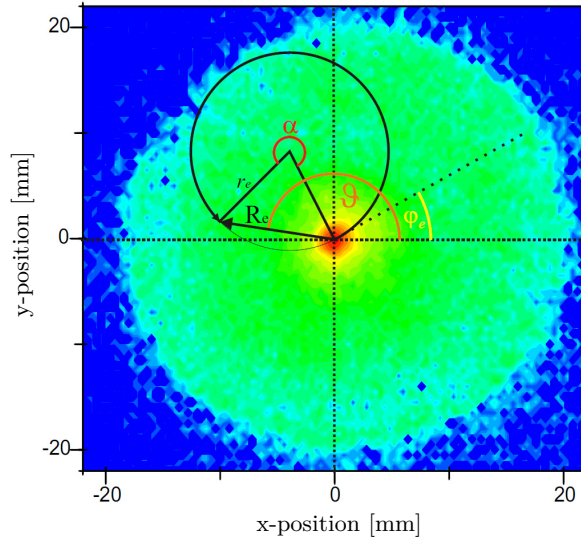


Figure 3.5: Electron position spectrum where the angles and vectors mentioned in the text are marked. The angle α could also have values higher than 2π . Due to the cyclotron motion, the number of counts in the centre is highest. The overall circle that is accessible to the electrons, with twice Larmor radius, is also visible. Figure courtesy of Schuricke [27]

After a time of $T = 2\pi/\omega$ the electron has performed a full turn which takes it back to the its starting position at $R = 0$ in the transverse plane. For times of flight that fulfil this condition, all information on transverse momentum will be lost, so care has to be taken to avoid these points. If they are not avoidable, several measurements with different combinations of magnetic field and extraction field can be used to ‘fill the gaps’. An actual advantage of this behaviour is the possibility to determine the absolute time of flight precisely, using the knowledge of the strength of the magnetic field. This allows avoiding systematic errors caused by delays that are not known precisely, for example from the projectile trigger to the arrival of the pulse in the target, or in the data acquisition chain.

Finally, we do not just want to obtain the magnitude of p_{\perp} , but also the initial emission angle ϕ_e of the electron in the perpendicular plane. To do so, the angle θ of the impact position is measured with respect to the centre of the detector picture, as shown in figure 3.5. Then, the time-of-flight value has to be used again to subtract the cyclotron motion:

$$\phi_e = \theta - \text{mod}(\omega t/2, 2\pi) \quad (3.13)$$

Using the modulus of 2π makes the expression valid even when more than one full turn is performed by the electron, which is usually the case in the experiment.

3.4 Projectiles

Owing to the open spectrometer, the apparatus is a relatively flexible system, allowing different kinds of projectiles to be used on its MOT target. In this work, a UV laser was employed for calibration measurements. The 3D-focusing configuration was designed for use with an electron gun, which gives a relatively large beam waist, causing a large reaction volume. The multiphoton and high energy photon regimes are explored with measurement campaigns at the free-electron laser FLASH in Hamburg.

3.4.1 UV laser

For calibration and testing purposes, an off-the-shelf microchip UV laser was used (*Teem Photonics MicroChip Series*). Its twice frequency-doubled Nd:YAG laser diode delivered a wavelength of 266 nm, generating a 9 kHz train of 400 ps pulses by passive

3. EXPERIMENTAL SETUP

Q-switching. Its wavelength makes the UV laser especially suited for photoionisation of laser-cooled lithium, as will be described in detail in chapter 5.

3.4.2 Electron gun

The electron gun is designed to deliver an electron beam of energies between 10–2000 eV (figure 3.6). The electron source is a tungsten filament which is heated by an electric current to induced thermionic emission. The electron cloud around the filament is concentrated by a Wehnelt cylinder, which can be also used to regulate or block the beam. Short electron pulses of the order of 10 ns can also be delivered by pulsing the voltage on the gating Wehnelt cylinder. Next come three rings that are used as lenses, the second and longest of which is the main focusing lens. Finally, the beam can be steered by four capacitor plates just before the exit pupil of the gun, while the whole gun can also be moved on a XYZ-manipulator. On the opposite side of the spectrometer, a Faraday cup is placed to capture the electron beam, preventing secondary events being created by stray electrons or the involuntary charging of insulators inside the vacuum chamber. The whole setup is quite difficult to align by event rate alone: The beam has to be guided through the spectrometer, where it should hit the centre of the MOT with the waist of the beam focus, before finally being dumped in the Faraday cup.

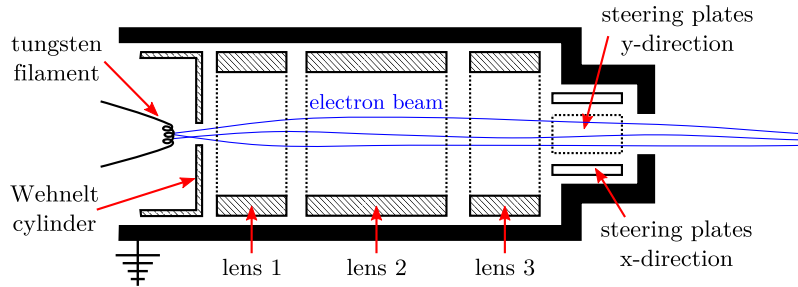


Figure 3.6: A schematic sketch of the electron gun.

Therefore, a beam monitoring screen was designed and built to be lowered into the spectrometer from the top, using the hole for the vertical MOT laser beam. It consists of a quartz plate ($35 \times 20 \times 2$ mm) on which a thin film of UHV compatible grease was spread out. A piece of copper mesh was pressed onto this layer and electrically connected to the holder with screws. This prevents the screen from charging up electrically.

Finally, a phosphorescing powder of the type used in TV tubes was applied uniformly and thinly. For electron beam energies above about 100 eV the beam profile and position can be observed visually or by a CCD camera. Thus the beam focus and overlap with the MOT can be optimised. The whole screen assembly sits on a long rotary-linear manipulator. In the topmost position, the screen can be stowed above the MOT coils by rotating it out of the centre position, opening the path for the vertical MOT laser beam.

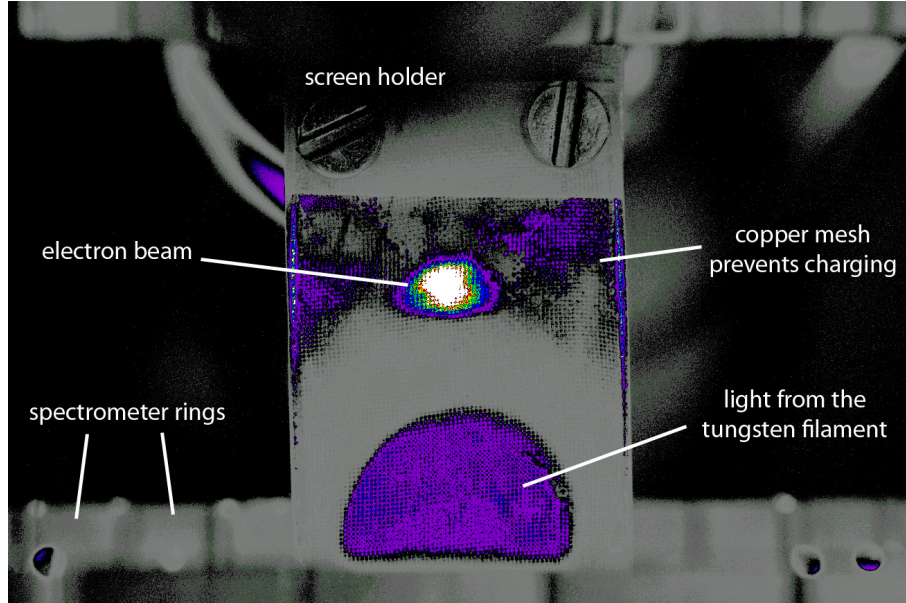


Figure 3.7: A false-colour image of the beam monitoring screen taken with the CCD camera that is also used to monitor the MOT. The gain for this image is quite high to show the surroundings, so that the phosphorescence caused by the electron beam is overexposed, which makes it look larger. The wire pitch of the copper mesh (0.2 mm) can be used as an absolute length scale. It has been verified that the beam can be focused down to a diameter of about 1 mm. The light from the glowing tungsten filament shining through the gun onto the screen is also seen; the electron beam position is higher up because the Helmholtz field is used to guide it through the spectrometer in an arc.

3.4.3 Free electron laser

The first free electron laser (FEL) was built by J. Madey and his team in the early 1970s, during his tenure at Stanford University [28]. Today, FELs deliver unprecedented laser intensities at high photon energies (FLASH: $I \geq 10^{14} \text{ W/cm}^2$, $E_\gamma = 30\text{--}300 \text{ eV}$). To create radiation of such properties, an operating principle very different from classical

3. EXPERIMENTAL SETUP

lasers is needed. As in a synchrotron, the magnetic deflection of an electron beam is used to generate *bremsstrahlung* photons; the big difference is that in an FEL, bunches of many electrons are made to emit these photons *coherently* (at least partially) by arrangements of alternating magnets, hence producing indeed *laser light*. Figure 3.8 shows a schematic picture of the setup. In first-order approximation, the magnet spacing translates into the laser wavelength by the Lorentz factor of the electron beam. By tuning the electron beam energy and thereby the Lorentz factor, the wavelength of the emitted light can be adjusted continuously. In practice, the electron wiggle motion has to be synchronised to the magnet spacing as well, so changing the strength of the magnets will also be required. In the details, running and tuning an FEL is a complex process with many parameters that can only be touched upon here. A theoretical description of the lasing process used at FLASH and other current high-gain FELs, the so-called self-amplified stimulated emission (SASE) of the electron beam was given by Zholents and Penn [29]. For the purpose of our experiment, we can simply treat the FEL as a light source with certain parameters, mainly wavelength, polarisation, pulse length, and pulse energy. Results from our beam time at FLASH in late 2010 will be presented in chapter 6.

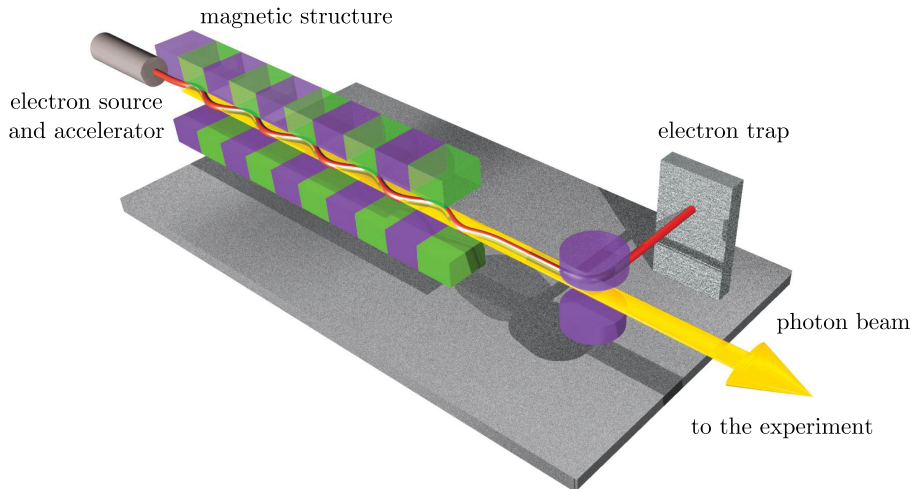


Figure 3.8: A schematic rendering of a free electron laser, picture courtesy of Hasylab.

3.5 Target preparation

The target in our experiment is a cloud of cold lithium atoms trapped in a MOT. It is loaded by decelerating a hot atom beam in a Zeeman slower, which can subsequently be captured by the MOT. During measurements, especially with the electron gun, the magnetic fields for the MOT and the Zeeman slower are turned off and an oven shutter is closed to prevent the hot lithium beam from entering the chamber. The target atoms are only trapped in momentum space by the lasers during this time, which means the cloud will expand with time according to its temperature. Therefore, ‘recapture’-cycles are performed, which consist of briefly turning on the MOT magnetic field to bring the atoms back together. Depending on the quality of the vacuum and of the MOT, as well as the switch-off time between recaptures, this can be done tens to many thousands of times. Only then the Zeeman slower and the oven beam have to be activated again to refill the MOT completely.

3.5.1 New oven and Zeeman slower

The original Zeeman slower for the experiment consisted of nine coil segments wound around a copper pipe, with copper discs separating them. The vacuum tube leading from the oven to the main experimental chamber would pass through the inside of the tube. Nine rack-mounted power supplies deliver the individual currents to generate the overall smooth magnetic field gradient. They can be switched by TTL signals, allowing automatic control of the magnetic field during a measurement cycle. The old slower was relatively heavy and there have been problems with the external cooling solution, causing some of the coils to fail. Anticipating further measuring campaigns in Hamburg, it was decided to build a new Zeeman slower with a simpler oven unit and a more reliable cooling solution. It is also slightly shorter and considerably lighter, the latter making transport easier and the former potentially improving the flux of lithium. The old cooling solution was having large copper discs between neighbouring coils, which would radiate the heat away. Some of these discs had been retrofitted with water cooling provided by copper piping that was welded on. In the new slower, the pipe with the coils and now much smaller discs is itself hollow and water-cooled directly. To ensure a good water flow along the whole length, two ridges are running between

3. EXPERIMENTAL SETUP

the outer and the inner wall of the tube in a double-helix shape, forcing the water to flow to the end of the slower and then back again.

3.5.2 Laser system

Figure 3.9 depicts a schematic diagram of the laser system used in the experiment. As explained in section 2.3, two different laser frequencies have to be provided, namely the cooler frequency for the $|2^2S_{1/2}, F = 2\rangle - |2^2P_{3/2}, F = 3\rangle$ transition and the repumper frequency for the $|2^2S_{1/2}, F = 1\rangle - |2^2P_{3/2}, F = 2\rangle$ transition. The first step is frequency-locking the master laser (*Toptica DL110 diode laser*, $P \approx 30$ mW). This is achieved by means of *Doppler-free saturated absorption spectroscopy* in a spectroscopy cell containing hot lithium vapour, giving a narrow and stable frequency standard. Because of the hyperfine splitting of the $2^2S_{1/2}$ ^7Li ground state of approximately 800 MHz, there is not just one lamb dip, but three: One each at the cooler and repumper frequencies, plus a third in the exact centre between the two, the so-called *crossover frequency* (described for example by Foot [22, pp.159–160]).

The crossover frequency is the one we use for locking the master laser. Its beam is then passed through a *tapered amplifier*, which gives an output power of about 400 mW after the optical isolator. The cooler and repumper frequencies are then produced using *acousto-optic modulators*; in order to reach the 400 MHz of shift that are needed, a 200 MHz AOM in double-pass configuration is used for each of the two frequencies. The AOMs can be controlled by TTL signals, making it possible to change the frequencies during a measurement cycle, for example to use different detunings for the MOT phase and the optical molasses phase. They can also be used as shutters to block the beam. The next critical step is overlapping the cooler and repumper beams again and coupling them into the single-mode polarisation-maintaining optical fibres leading to the experiment.

For each MOT axis, a fibre outcoupler is installed in front the respective MOT window, while a retro-reflecting mirror is mounted on the opposite side. They are adjusted so that the initial and reflected beam overlap. A $\lambda/4$ wave-plate is installed between the outcoupler and the window to achieve the correct circular polarisation. After all three beams are aligned, the optical molasses setup is complete.

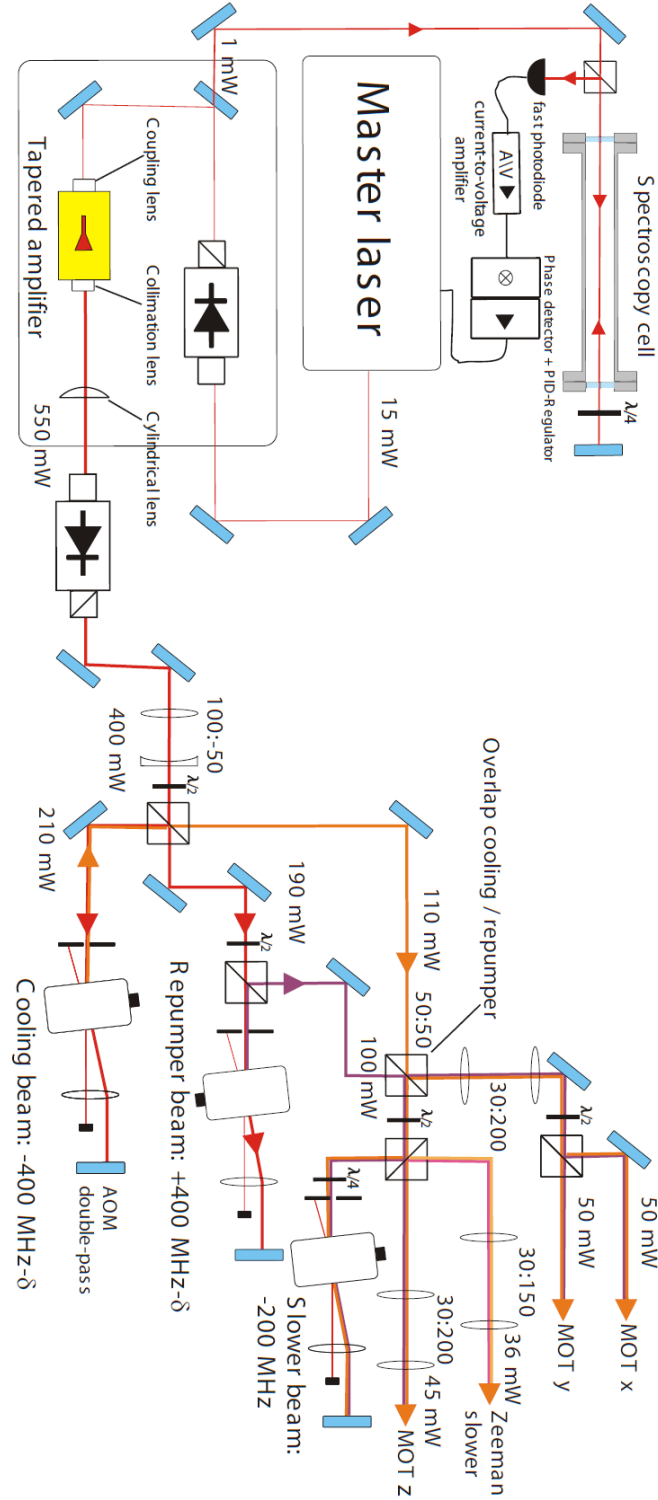


Figure 3.9: The laser system which provides the MOT and Zeeman slower beams.

3. EXPERIMENTAL SETUP

3.5.3 MOT-field generation and switching

The coils generating the MOT magnetic field and the electric circuitry to switch it are both very critical for the performance of the experiment. The two main goals are fast switching times and as little a negative effect on the ultra-high vacuum as possible. The former makes it possible to load the MOT, switch off the magnetic field during the measurement, and then recapture most of the atoms.

The duty cycle for data acquisition is greatly improved by this technique, especially when many thousands of recaptures are possible. Also, a fast switch-off time yields a smaller and denser target during the data acquisition phase, since the cold atomic cloud has not yet expanded much.

The quality of the vacuum determines the losses and the lifetime of the MOT; a pressure better than at least 10^{-9} mbar is needed for efficient MOT operation. To realise an *optical dipole trap*, as has been achieved with this experiment before (continuing work by Hubele [30]), even better vacua in the 10^{-11} mbar-range are needed. This limits the choice of materials for the coils and makes water-cooling imperative, since the required currents of up to 60 A would lead to considerable heating and thereby outgassing of the coils. These constraints have led to a general design consisting of an aluminium rim on which a coil of copper tube is wound. The loops are electrically insulated against each other and the rim by polyimide film (Kapton), which is layered around the copper tube during the winding of the coil.

For fast switching *of the current*, the performance of the electric circuits is important. There are mainly two practical solutions for switching the required currents in times under $100\ \mu\text{s}$: Combining several power MOSFETs (metal oxide semiconductor field-effect transistor) or using modules of IGBTs (insulated gate bipolar transistor). The circuit for our experiment uses IGBTs and has several interlock features to protect the hardware from erroneous pulse sequences or other harmful operating conditions. It features a large water-cooling solution and was constructed by the institute's electronics department [20].

The falloff *of the actual magnetic field* is however not only influenced by the switching of the coil current. It is also governed by *eddy currents* induced in the surroundings of the coil during switching, especially in the rim. These eddy currents can have a lifetime that is much longer than the current shutdown time. To minimise this effect, the rim

is slotted to prevent having a large closed loop. Similarly, the spectrometer rings are divided into sections.

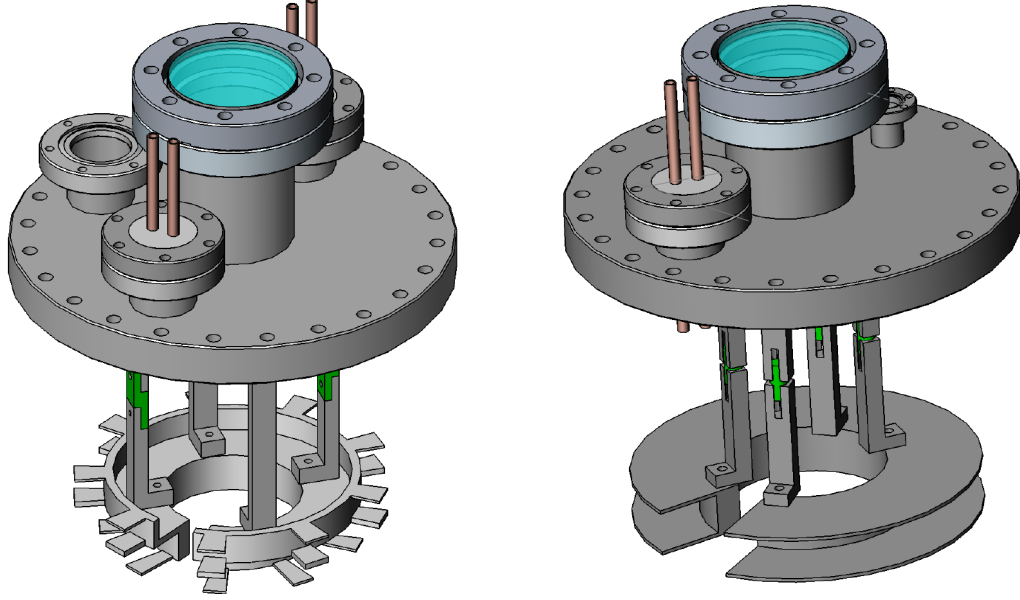


Figure 3.10: The rim for the new coils (left) in comparison to the old design (right). On the new rim, the MOT coil (bottom) and the compensation coil (top) will be wound between the metal flags. Both can be connected independently via a dedicated double electrical feedthrough. The old rim houses only a MOT coil with a larger diameter.

Despite these efforts, the switch-off times were still not completely satisfactory: While the current is switched in less than $80\,\mu\text{s}$, the residual magnetic fields caused by the eddy currents only become negligible for electron measurements after more than 2 ms. It was therefore decided to build a new pair of MOT coils, with an overall smaller and more open rim, to reduce both the eddy currents and allow better pumping. Figure 3.10 shows the old and new coil rim designs side by side. Another idea that was incorporated in the new design is the *compensation coils*. These are another pair of coils of bigger diameter above and below the MOT coils, with inverted magnetic field. This addition keeps the magnetic field gradient at the position of the MOT the same, while reducing the field in the far region. The compensation coils are electrically connected in series with the main MOT coils, which means that the current passing through them is the same as in the main coils, allowing the use of the same circuitry as before. The result is a greatly reduced magnetic field at the chamber walls compared

3. EXPERIMENTAL SETUP

to the same situation without compensation coils. Also, the overall energy stored in the magnetic field is lowered. In section 5.3, the characterisation measurements of the new coils will be presented.

4

Designing the focusing lens

The momentum resolution of a reaction microscope is limited by several factors. The most important ones are generally the target temperature, the target size, the field homogeneity in the spectrometer, and the precision of the timing measurements. Using a MOT, our experiment is not limited by the target temperature: At a red-detuning of 2–3 linewidths, a temperature of about $500\text{ }\mu\text{K}$ is reached, translating into negligible momentum spread of 0.004 a.u. for the lithium atoms. For the longitudinal momentum p_{\parallel} , the time-focusing geometry reduces the spread in times of flight due to the target size, limiting it to under ten nanoseconds, which corresponds to a momentum spread of less than 0.008 a.u.

For the transverse momentum p_{\perp} on the other hand, the target size has a noticeable effect: An extension of 1 mm leads to an uncertainty in transverse momentum of about 0.043 a.u. at an extraction voltage of 0.1 V/cm, which grows to 0.43 a.u. at 10 V/cm. As it is the biggest source of error, the idea is to use an electrostatic focusing lens to project the ions onto the detector according to their recoil momenta, regardless of their starting position within the target.

This idea is not new, but the technical realisation has proved difficult. The lens creates inhomogeneous field lines that can disturb the trajectories of the ions, especially shortly after their creation in the target, when they are slow. The lensing field should therefore be kept away from the interaction point. One method is using metallic meshes before and behind the lens in order to keep the bent electric field lines well contained [31]. Unfortunately, this also decreases overall detection efficiency, which is very crucial when multi-particle coincidences and multiply differential cross-sections are measured. This

4. DESIGNING THE FOCUSING LENS

possibility was therefore excluded. Another problem with electrostatic lenses is that they often have strong aberrations when the beam to be focused does not pass through close to the central axis of the lens. Therefore, a big lens should be employed, so that only the central part has to be used.

Experimentally, the design was constrained by the fact that we did not want to change the basic structure of the spectrometer. In an earlier attempt on this experiment with spatial focusing, one spectrometer ring was connected to a separate power supply to act as the electrode for the electrostatic lens, but the results were not convincing. Even after careful simulations, having more overall flexibility would be advantageous. Therefore, ten rings and the drift tube were independently connected to the outside of the vacuum chamber via a multi-feedthrough flange. An external voltage divider allows the operation without lens using the same power supply as before, and for lens operation only one additional power supply is needed. Different rings can be used as the lens and the drift length is easily changed. The spectrometer can still be operated in pure TOF-focusing mode like before, which gives the best measurement of the absolute times of flight for different ion species and can serve as a calibration for other measurements. The change between these modes is fast and only requires re-plugging a few cables, leaving the vacuum and everything else intact.

4.1 Introduction to electrostatic lenses

In 1927, H. Busch showed that an appropriate axially symmetric magnetic field can act on rays of charged particles in a similar way as a glass lens acts on light rays [32]. In the early 1930s, Davidson and Calbrick recognised this was also true for axially symmetric electric fields. Another pioneer, both theoretically and experimentally, was E. Brüche, who used an electrostatic lens in an *electron microscope* for the first time [33]. There are many similarities between optical and electrostatic lenses, but also marked differences. One such difference is that in light optics, a lens is made from a material with a certain refractive index that can be shaped arbitrarily. The index of refraction changes the wavelength of the light in that region. The equivalent in electrostatic optics is the electrostatic potential—it also changes the energy, or wavelength, of a charged particle. In contrast to light optics, the equipotential lines cannot have an arbitrary shape, but

must arise from a given charge distribution. This makes the control of aberrations more difficult. Also, the density of the potential lines cannot change as abruptly as the refractive index does, for example, at a glass–air interface. A high-transmissivity mesh would provide the closest analogy to such a surface. Figure 4.1 shows a simple electrostatic lens, the so-called einzel lens, in accelerating and decelerating configuration. It consists of three cylindrical electrodes, the first and the last of which are grounded while a positive or negative voltage is applied to the middle one. Both signs of the voltage provide focusing. The net speed change caused by the lenses is small as the timing markers indicate, but the time of flight depends on the radial position of the particle, highlighted by the ‘bent wavefront’ after the lens. This can be taken into account and corrected for, should the effect become important in experimental situation.

In the 1960s, applications at particle accelerators sparked more theoretical interest in electrostatic lens performance and aberrations. For several special rotationally-symmetric lens shapes, analytical calculations of aberration parameters were made, for example by Septier [34] at CERN. With the arrival of more powerful computers, numerical simulations became feasible and gradually lifted the restrictions on electrode shapes. Today, construction files of an experiment can be exported from a CAD program and are rasterised. Even big parts can be simulated with millimetre-resolution in a reasonable time frame on standard PC hardware, allowing a flexible design approach. One of the software packages routinely employed for such calculations is the *Simion* program [35], first developed by McGilvery in the late 1970s McGilvery [36]. It was used for the simulations described in the next section.

In *Simion*, the geometry of the electrostatic problem is represented by so-called *potential arrays*, a 3D-grid of small cubes which are all either defined as an electrode or free space. The user has to set the voltages on all electrode points, while the resulting electric fields in the free regions are calculated by *Simion*. It first computes the electrostatic potentials in the free regions by solving the Laplace equation using an optimised over-relaxation finite difference method [35]. Then the electric field can be derived by taking the gradient of the potential. Finally, *Simion* calculates the trajectories for particles of given masses, charges, starting positions and initial momenta. The trajectories are computed relativistically using fourth-order Runge-Kutta techniques [35].

4. DESIGNING THE FOCUSING LENS

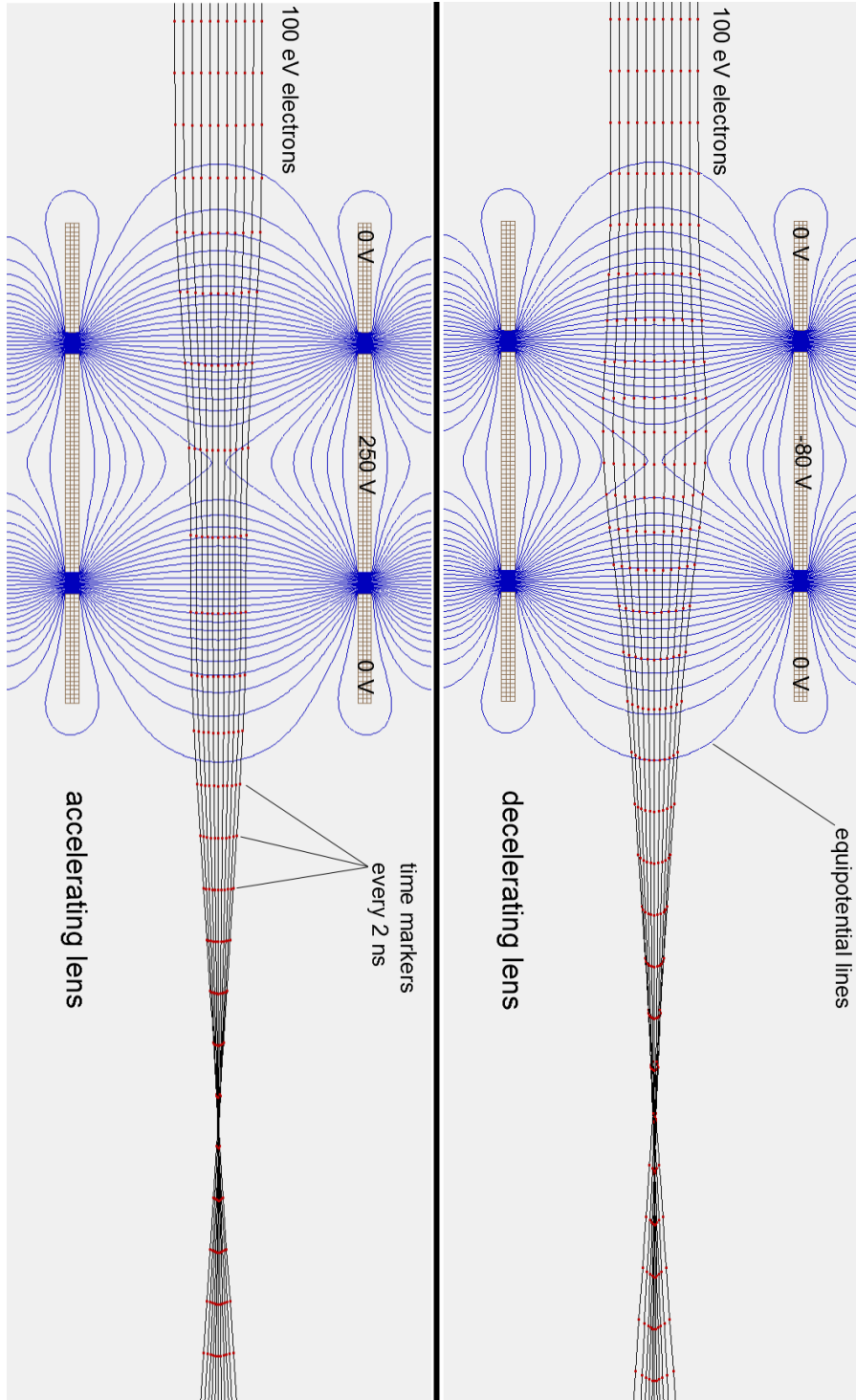


Figure 4.1: An accelerating and a decelerating einzel lens simulated by *Simion*. The lens cylinder diameters are 64 mm, the electrons each start 2 mm apart from each other.

4.2 Identifying constraints and performance parameters

Figure 4.2 shows the central part of the spectrometer (compare figure 3.2). There is an aperture mounted on the last open ring on the ion side to keep the bent field lines of the lens away from the reaction volume. The internal and external electrical connections are shown as well; the latter allow using any of the second to tenth closed ring after the aperture as the lens electrode.

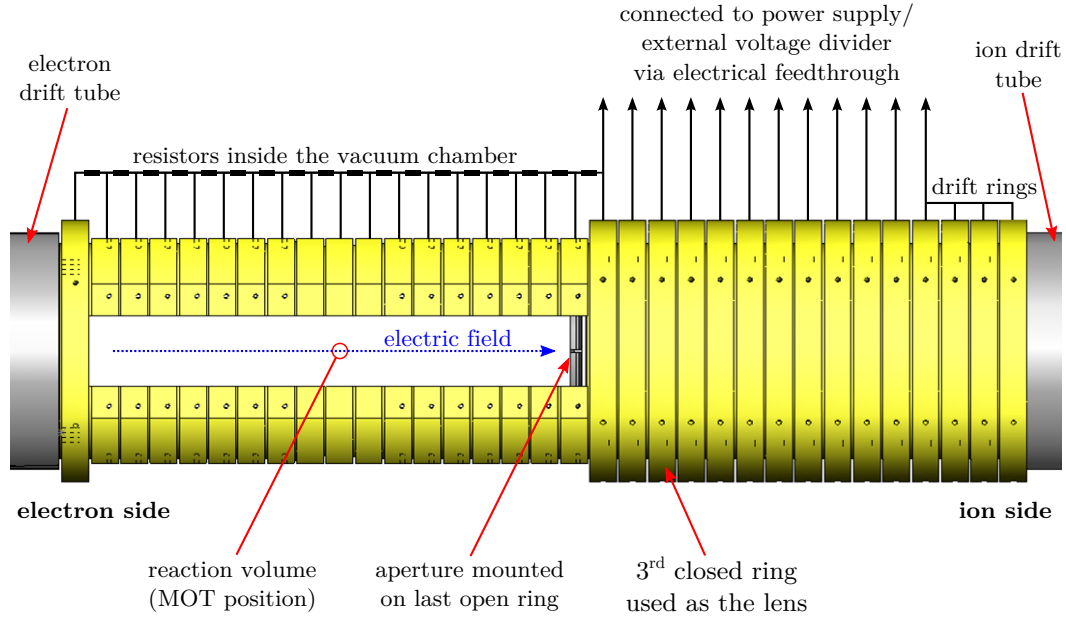


Figure 4.2: Closeup of the central part of the reaction microscope. The third ring after the aperture that is later chosen as the best lensing configuration is marked. The ion trajectories would be parabolae opening towards the ion detector on the right, while the electron trajectories would be spiralling to the left under the influence of the Helmholtz magnetic field (not shown).

The performance of the different lensing configurations differs mainly in three aspects: The curvature of the focal plane, i.e. how much the outer part of the detector image is out of focus when it is optimised for centre sharpness; how far the bent field lines from the lens protrude into the central part of the spectrometer, possibly disturbing the slow ions immediately after ionisation; lastly, how well the TOF-focus is maintained with respect to the standard configuration. A few general results were quickly found:

4. DESIGNING THE FOCUSING LENS

First, an accelerating lens is superior to a decelerating one. The latter has a more curved focal plane, and in the real experiment the slow ions are more easily influenced by stray fields or other outside influences.

Second, using too small an aperture causes the system to become very sensitive to small deviations from the axial symmetry. This might even have been one of the main problems of the earlier attempts. It is better to have a bigger aperture and only use the inner half of the radius for the ions to travel through. When taking measurements with the the lens, care should be taken to properly centre the MOT, and to make sure the extraction voltage is not too low, even if this means not using the whole area of the detector. Third, the position of the spatial focus is nearly independent from the particle energy, i.e. at a setting that focuses particles of a certain momentum well, particles with smaller momentum are also focused.

To quickly and systematically evaluate the performance of different configurations, and get an intuition for the results, I devised a few simple test patterns.

4.2.1 Pattern for testing TOF focus

This pattern consists of a number of particles starting evenly spaced along the spectrometer axis, all with the same initial momentum, as shown in figure 4.3. It allows the easy verification of time-of-flight focusing, using the option of drawing time markers for every particle at fixed intervals. The distance at which the positions of all particles from the original line coincide is the TOF-focusing distance, or focal length. Without the lens, this distance is reached at $d = 2a$, i.e. after the particles have drifted for twice the acceleration length, as demonstrated in section 3.1.

Without the lens, the distances between the particles in the line distribution stay constant until the end of the acceleration length, where the packet starts to shrink. After being reduced almost to a point at the end of the drift area, the packet becomes longer again, with the order of the particles reversed from their starting order. When using an accelerating lens, time-of-flight focusing is achieved at a later point, behind the detector plane, so the drift length has to be increased. Small changes of the lens voltage around its operating point cause only a negligible shift of the time-of-flight focus position.

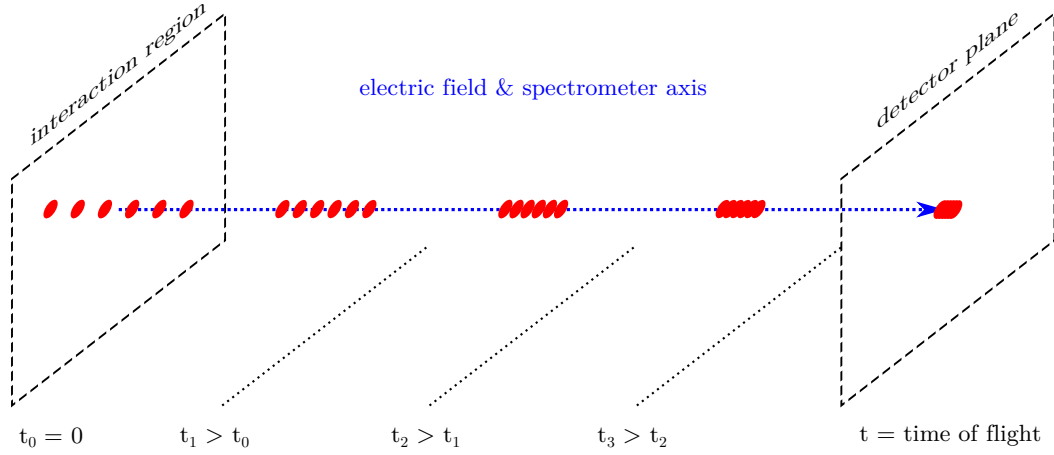


Figure 4.3: The pattern to test for time-of-flight focusing. Here, the initial momenta of the particles are all zero. It is a simplified picture; in the real spectrometer and the simulation, the distances between the particles only start shrinking when entering the drift area.

In the experiment, the drift length can only be changed in steps of full rings as the spectrometer geometry is fixed. Also, the position of the aperture and lens cannot be chosen freely, but are constrained to a position on a ring. The lens voltage is then determined by the demand of spatial focusing. It was found that the free, continuous parameter that can be optimised here is the *aperture diameter*. In the first simulations that were done, it was set to 30 mm, which seemed like a good compromise between keeping the field distortions from the lens away from the interaction region, and having the ions not pass too close to the edges of the aperture. However, this geometry showed TOF back-focusing with one ring added to the drift length, but TOF front-focusing of similar magnitude with two rings added to the drift length. 30 mm diameter are therefore an ‘unfortunate’ setting. A series of simulations with different diameters were made, which is numerically costly: For each change in the geometry of the spectrometer, the electrostatic problem has to be solved again by *Simion*, which takes about an hour on a standard desktop computer with the geometry resolution of 1 mm that was used. Table 4.1 contains simulation data on the shift of TOF focus for different aperture diameters. It was found that a diameter of 42 mm with two rings added to the drift length came close to perfect TOF focusing in the detector plane when using the third ring behind the aperture as the lens. Table 4.2 contains results on the TOF focusing performance for different lens and drift combinations with the 42 mm aperture.

4. DESIGNING THE FOCUSING LENS

aperture \varnothing	$\Delta\text{TOF-focus}$	l_{det}	mean TOF	ΔTOF
25 mm	−22.8 mm	0.10 mm	88.66 μs	9.0 ns
30 mm	−16.6 mm	0.07 mm	88.60 μs	6.3 ns
35 mm	−12.5 mm	0.05 mm	88.53 μs	5.3 ns
40 mm	−6.2 mm	0.03 mm	88.46 μs	2.6 ns
42 mm	−3.7 mm	0.02 mm	88.43 μs	1.9 ns

Table 4.1: Simulation data on TOF-focusing with different aperture diameters. For each simulation, the third ring behind the aperture was used as the focusing lens. The lens voltage was kept constant at $U_{\text{lens}} = -13.75\text{ V}$, which provided adequate spatial focusing for all diameters. The $\Delta\text{TOF-focus}$ value is the position of the best time-of-flight focusing with respect to the detector plane at $z = 794\text{ mm}$ from the interaction point; negative numbers signify front-focus. The string of particles at the starting position was 2 mm long; l_{det} is its extension at the detector position. A reduction of the effective target size in longitudinal direction by a factor of 100 is achieved with the 42 mm aperture.

4.2.2 Pattern for testing spatial focusing on the X- and Y-axis

A cross-shaped pattern, illustrated in figure 4.4, is used to verify spatial focusing for a certain momentum vector. The complete cross should be projected onto a single point at the detector with perfect focusing. Choosing an appropriate lens voltage, it can indeed be seen that the cross becomes smaller after the lens until it is nearly a point at the detector plane. An unwanted effect is that focusing in X- and Y-direction are not always reached in the same position. This turned out to depend on the potential on the boundary of the simulation, corresponding to the ground potential of the chamber in the experiment. The outside field lines seep into spectrometer through the open sides and turn it into a cylinder lens. By shifting the position of zero potential in the spectrometer, it is possible to achieve even focus for both directions. In the experiment, this can be done by shifting the spectrometer voltages applied at each end versus ground as a whole. Another technical countermeasure that will be implemented in the near future is fixing long metal ‘flags’ at the edges of the spectrometer openings. They will be on the same electric potential as the spectrometer rings they are fixed to, keeping the outside field lines further away from the spectrometer axis, while also leaving the paths for the MOT lasers open.

Several cross pattern groups with different momentum *directions*, for example up, down, left and right, can be used to determine changes in focusing behaviour across the

4.2 Identifying constraints and performance parameters

lens pos.	+drift	U_{lens}	$\Delta\text{TOF-focus}$	l_{det}	mean TOF	ΔTOF
no lens	0	—	−33.3 mm	0.13 mm	87.95 μs	11.5 ns
1 st	0	−12.76 V	> 15 mm	0.32 mm	86.40 μs	26.9 ns
1 st	1	−12.81 V	> 15 mm	0.15 mm	87.61 μs	12.0 ns
1 st	2	−12.87 V	−13.8 mm	0.06 mm	88.94 μs	5.4 ns
2 nd	0	−14.57 V	> 15 mm	0.40 mm	85.93 μs	33.6 ns
2 nd	1	−14.72 V	> 15 mm	0.22 mm	87.12 μs	19.3 ns
2 nd	2	−14.80 V	+4.9 mm	0.03 mm	88.45 μs	2.4 ns
3 rd	1	−13.70 V	> 15 mm	0.17 mm	87.13 μs	16.3 ns
3 rd	2	−13.75 V	−3.7 mm	0.02 mm	88.43 μs	1.9 ns
4 th	1	−16.37 V	> 15 mm	0.16 mm	86.98 μs	14.4 ns
4 th	2	−16.41 V	−7.9 mm	0.03 mm	88.31 μs	3.4 ns

Table 4.2: Simulation data for different lens positions and drift lengths. The 42mm aperture is used and placed in the last open ring of the spectrometer on the ion side. The ion pattern consisted of 11 ions with $m = 7\text{amu}$ and no initial momentum. They were each spaced 0.2mm apart along the spectrometer axis, around the nominal target position, giving an initial packet length of 2mm. The spectrometer voltages were +2.25 V on the electron side and $-5/-4.75/-4.5$ V on the ion side, depending on the number of spectrometer rings added to the drift length. The voltage step per ring was 0.25 V, corresponding to an electric field of 0.25 V/cm.

The name of the lens position tells how far the lens is positioned from the aperture, i.e. ‘1st’ is the neighbouring ring, ‘2nd’ is one ring further towards the detector, etc. The column ‘+drift’ shows by how many spectrometer rings the drift length has been prolonged. The *lens operating voltage* U_{lens} is the voltage that has to be applied in order to focus a spatial distribution of ions at rest onto the smallest possible point in the detector plane. The *TOF focus deviation* $\Delta\text{TOF-focus}$ is the position of the best time-of-flight focusing with respect to the detector plane. Negative distances mean early focus (front-focus), positive distances late focus (back-focus). If the position of the focus lay more than 15 mm behind the detector plane, it was outside the simulation area and could not be determined. The packet length at the detector l_{det} highlights the effect of compressing the effective target size. The absolute minimal packet length is < 0.01 mm, or shorter than 1 ns, but in practise the distance target–detector is only known with an accuracy of about 5 mm, making such an exact application of the simulations impossible. This means the focus position and ΔTOF have systematic errors of at least 5 mm and 2.5 ns when comparing with the experiment. The mean times of flight show the influence of the accelerating lenses and differently sized drift lengths. The value ΔTOF is the difference in time-of-flight between the first and the last of the 11 ions in the packet.

4. DESIGNING THE FOCUSING LENS

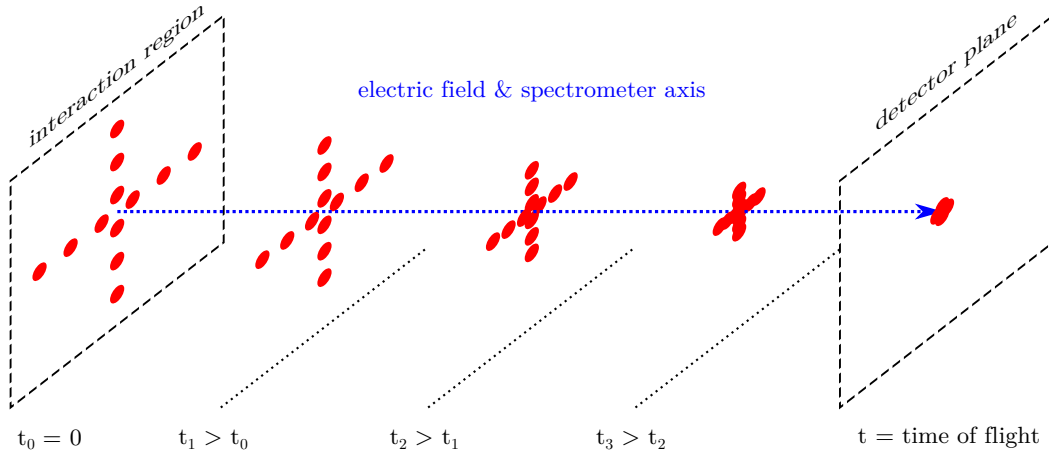


Figure 4.4: Particles in a cross-shaped pattern, evenly spaced in X- and Y-direction, all with the same initial momentum (being zero in the drawing).

detector plane. It turns out that the focus on the spectrometer axis is always reached later than off-axis. The difference becomes larger, i.e. the focal plane is more curved, when the lens is too close to the aperture; the field lines also look quite asymmetric in that case. Focal plane curvature also increases when a ring too close to the detector is chosen, since the required focal length becomes shorter. The voltage needed to achieve focusing in the detector plane also grows considerably with the higher particle speeds encountered in those positions, as the time spent in the lens area decreases. Figure 4.5 shows the results of a simulation using the cross pattern with settings very similar to the ones used in the experiment with the UV laser. Each point in the starting pattern contains five ions with different momenta (up, down, left, right, zero); when they reach the detector, they arrive grouped according to their momenta, each of the five momentum groups mimicking the shape of the starting pattern. Focal plane curvature and uneven focus are minimised and not visible.

4.2 Identifying constraints and performance parameters

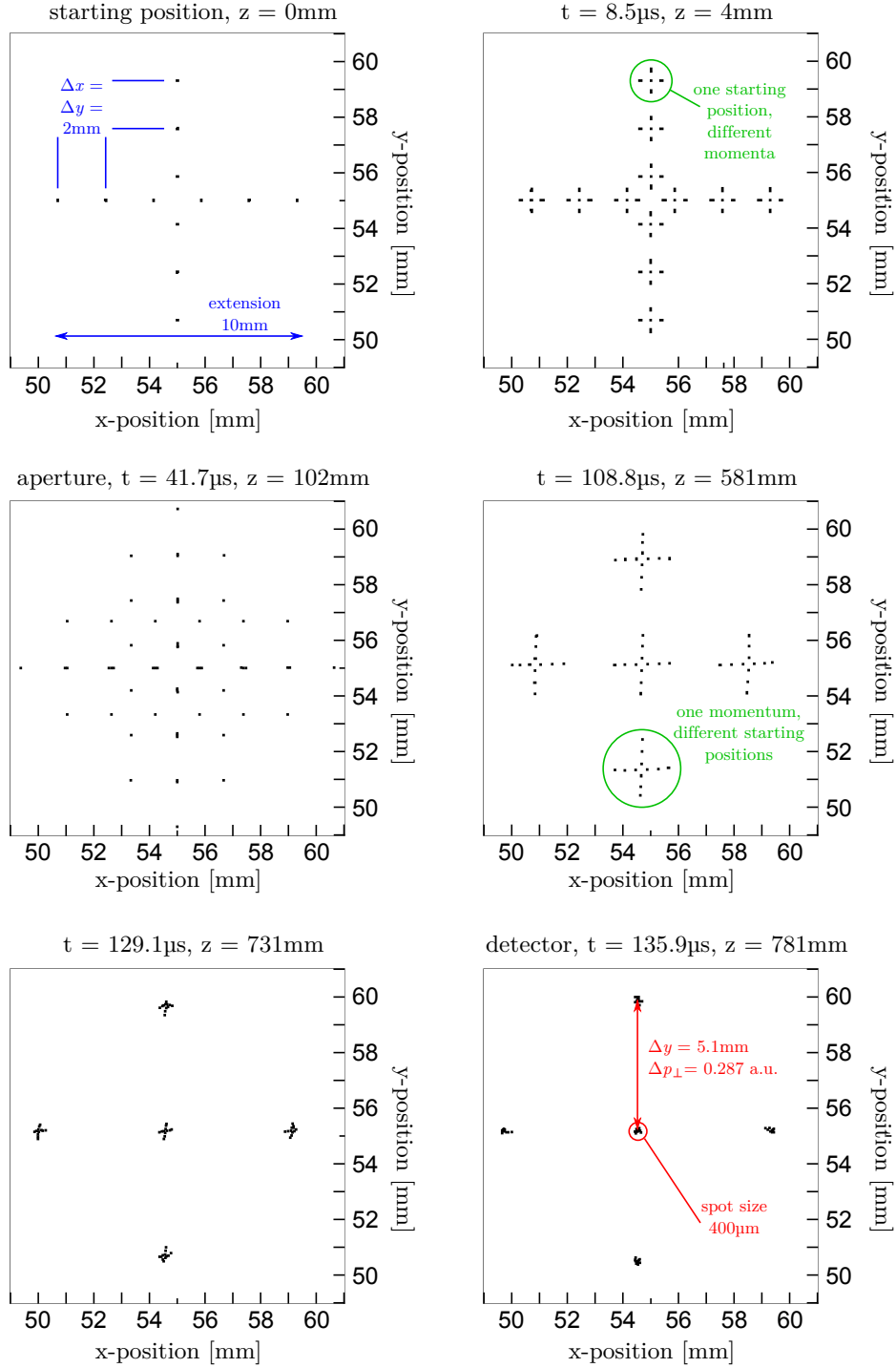


Figure 4.5: Simulation data for spatial focusing. The spectrometer voltages were $+0.9\text{ V}$ (electron side) and -2 V (ion side) at 0.1 V/ring . The lens was set at -5.4 V , using the third ring from the 42 mm aperture. These settings emulate the experimental conditions during the UV laser measurements (chapter 5).

4. DESIGNING THE FOCUSING LENS

4.2.3 Pattern for testing focal plane curvature and image shape

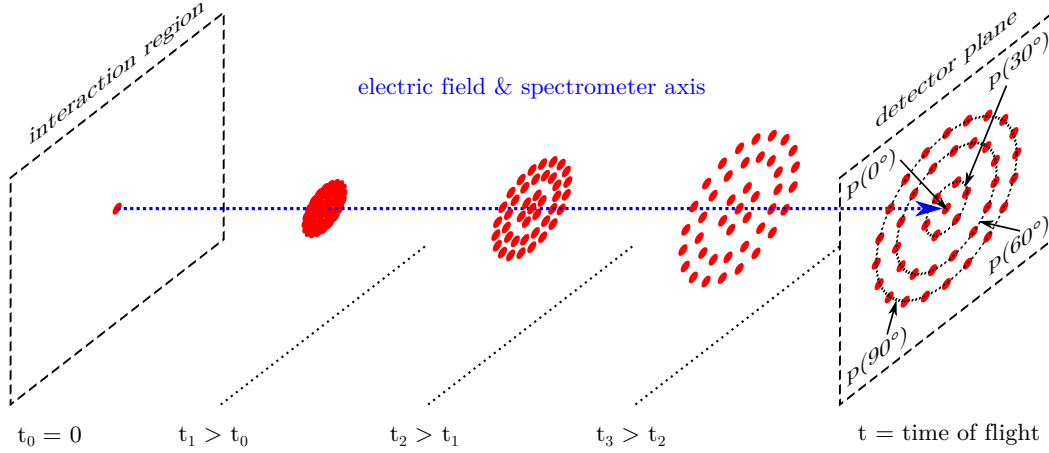


Figure 4.6: All particles are starting from the same spot with the same absolute momentum; the momentum directions are arranged in cones around the spectrometer axis.

To test the shape of the position image and of the focal plane, particles starting at a single point with their momenta arranged in cones were used. The absolute momentum was the same for all particles; the cone opening angles were between 0° (towards the detector) and 180° (away from the detector) in steps of 15° . The cone at 90° (actually a circle) gives the maximum size of the detector image at the given particle momentum. This configuration can also be used to verify that the times of flight are indeed constant for each cone within a few nanoseconds, not depending much on the transverse momentum. Furthermore, the cones convey a good visual understanding how the different angles are projected onto the detector. Any ellipticity of the position image can be spotted as well.

When the starting point for the simulated particles is changed from a point to a Gaussian distribution, the position image of the cones on the detector becomes fuzzy without focusing. Using the lens, the cones show in an intuitive way how the detector image depends on the lens voltage—starting from a low value, the outermost ring comes into focus first as the voltage is increased. The focus then moves inward as more voltage is applied. The effect of the open spectrometer is also seen: When the outside electrical potential is shifted with respect to the spectrometer voltages, the rings in the position image on the detector become elliptical. Furthermore, different focal distances along

the X- and Y-axes become visible as a ‘sharp axis’ and an ‘unsharp axis’ of the ellipses.

4.3 The resulting design

Based on the results of the simulations, the choice for the final lens configuration was made. The last open ring is the furthest away from the interaction point we can put the aperture for technical reasons; it gives the best shielding of the interaction region from the lens’ influence. The lens itself has to be placed far enough from the aperture to avoid focal plane curvature due to the asymmetric lens, yet it cannot be too far from it because curvature would increase again as it gets closer to the detector. The simulations presented in table 4.2 show that the third ring after the aperture is in a ‘sweet spot’, requiring less lens voltage than both its neighbours. Optimising TOF-focusing for the third-ring case yields usable aperture diameters of 26 and 42 mm.

These two sizes were therefore machined and gold-plated. The 42 mm aperture will be the more robust choice as this configuration is disturbed less by deviations of the experiment from the axial symmetry. It was consequently installed for the characterisation measurements. The 26 mm aperture could be used to block out more unwanted events by leaving a smaller opening around the spectrometer axis. Figure 4.7 shows the equipotential curves for the 42 mm configuration.

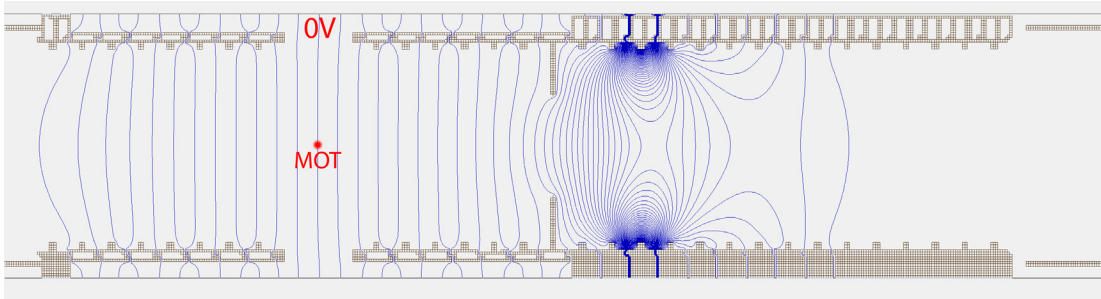


Figure 4.7: The spectrometer with the final lens design (42 mm aperture) used for the measurements in the next chapter. The spectrometer voltages were -1.8 V on the ion side with two rings added to the drift length, 0.9 V on the electron side and the lens at -5.4 V. The equipotential lines are each 0.07 V apart, with the zero position marked. The MOT is practically on the 0 V line.

4. DESIGNING THE FOCUSING LENS

5

Measurements

In the first part of this chapter, the characterisation measurements of the 3D-focusing spectrometer will be presented. The spatial- and time-focusing performance was tested using a linearly polarised UV laser on an optical molasses target, generated by switching off the MOT magnetic field during data acquisition. In the second part, data on the falloff time of the magnetic field with the new pair of MOT coils are shown and compared to the old configuration, also disentangling the effects of the new compensation coils.

5.1 Testing the spatial focusing

The main application of the spatial focusing lens will be measurements where the projectile beam is considerably spread out, such as unfocused light beams (for example by Zhu et al. [37]) and electron beams. The beam from our electron gun, for example, has a relatively big diameter (between one and a few mm) compared to the focused lasers typically used. Furthermore, it transverses the target perpendicular to the spectrometer axis; therefore, the target extension along the beam axis determines the length of the collision region. The simulations show that the focusing lens can correct for this, but characterisation measurements are of course needed.

These were done using a pulsed UV laser (Q-switched, twice frequency-doubled Nd:YAG laser diode at 266 nm) with a repetition rate of 9 kHz and a pulsewidth of about 400 ps. The wavelength corresponds to a photon energy of 4.66 eV which is below the ionisation threshold of the lithium ground state of 5.39 eV. It is however sufficient to ionise the $2^2P_{3/2}$ state at 3.54 eV below threshold, which is populated during the laser cooling

5. MEASUREMENTS

cycle. The electron excess energy of 1.12 eV translates into a recoil ion momentum of 0.287 a.u.:

$$p_{\text{Li}} = p_e \approx \sqrt{2m_e E} \equiv \sqrt{2m_e \frac{E}{E_H}} = \sqrt{2 \times \frac{1.12 \text{ eV}}{27.21 \text{ eV}}} = 0.287 \text{ a.u.} \quad (5.1)$$

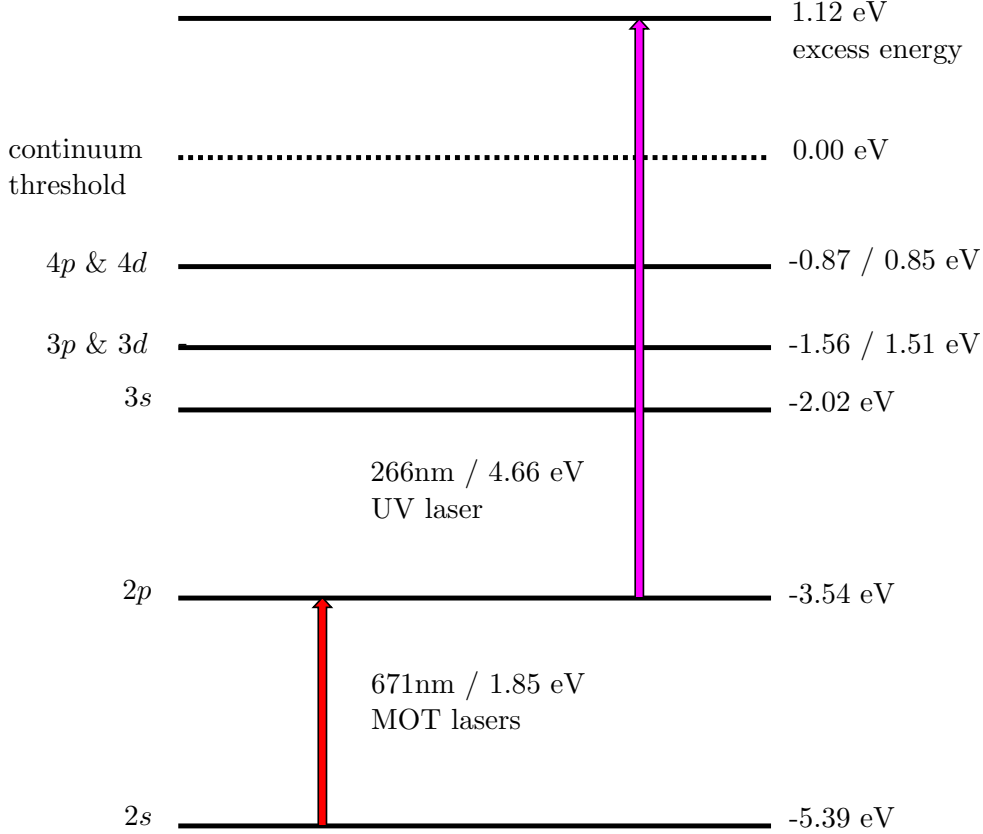


Figure 5.1: Simplified level scheme of ${}^7\text{Li}$, linear scale. Energy level data were taken from the NIST reference tables, based on work by Radziemski et al. [38].

This is quite a small value, corresponding to a recoil ion speed of only 49 m/s, but the excellent momentum resolution of the machine (0.04 a.u. for p_{\parallel} and 0.08 a.u. for \vec{p}_{\perp} , see Schuricke et al. [39]), due to the cold target and large spectrometer, enables the measurement. One big advantage of the UV laser is the large photoionisation cross-section for Lithium in the 2p-state, measured to be $8.4 \pm 1.4 \text{ Mb}$ at 266 nm [40]. It is also very selective, since no other components of the residual gas can be ionised at this

comparatively low photon energy. Compared with the electron gun, not being susceptible to magnetic fields, transferring a very well-defined energy to the target atom and being able to control the polarisation of the beam are further advantages. One disadvantage for demonstrating the focusing effect of the lens is the relatively small effective diameter of the beam. It appears to be elongated (approximately elliptical with a ratio of 1:4), but checking with an iris and a power meter shows that more than half of its intensity lies within a small circular centre. Furthermore, the default polarisation is linear along the small axis of the elongated beam, making it harder to see the effects of the size. A zero-order $\lambda/2$ waveplate was used to turn the polarisation axis by 90 degrees.

The first series of measurements was to confirm the spatial focusing of the electrostatic lens and find the best parameters for its operation. Six different lens voltages and the old spectrometer configuration without a lens were measured, within a time of about 12 hours. All other experimental settings were kept the same, and the consistent position and properties of the MOT and the optical molasses were monitored with a CCD camera that can be triggered at the desired time in the measurement cycle (especially during the data acquisition phase). To create a virtual bigger reaction volume that makes the focusing effect more visible, the laser beam was moved up and down along its polarisation axis, and every lens setting was measured in each of the three positions (up, middle, down). Later, the data were combined, thus simulating a bigger target. Care was taken to use the same number of events from each position setting to give them the same statistical weight. The resulting raw spectra for the detector hit positions, shown in figure 5.2, exhibit two lobes along the polarisation axis of the UV laser. Next, a cut on the times of flight of 200 nm around the centre of the distribution was applied in order to select the events with the biggest \vec{p}_\perp ; the resulting spectra are shown in the bottom row of figure 5.2. Most of the events from the centre, which have low \vec{p}_\perp , have been removed by the procedure. The total size of the image was taken as the distance of the two lobes. The outer edge of the bottom lobe was finally used to determine the resolution of the picture, given by the rise distance σ_{rise} in relation to the total image size; the results are shown in table 5.1. Figure 5.3 illustrates the extraction of the resolution in the reference setting and with the lens set to -2.82 V.

5. MEASUREMENTS

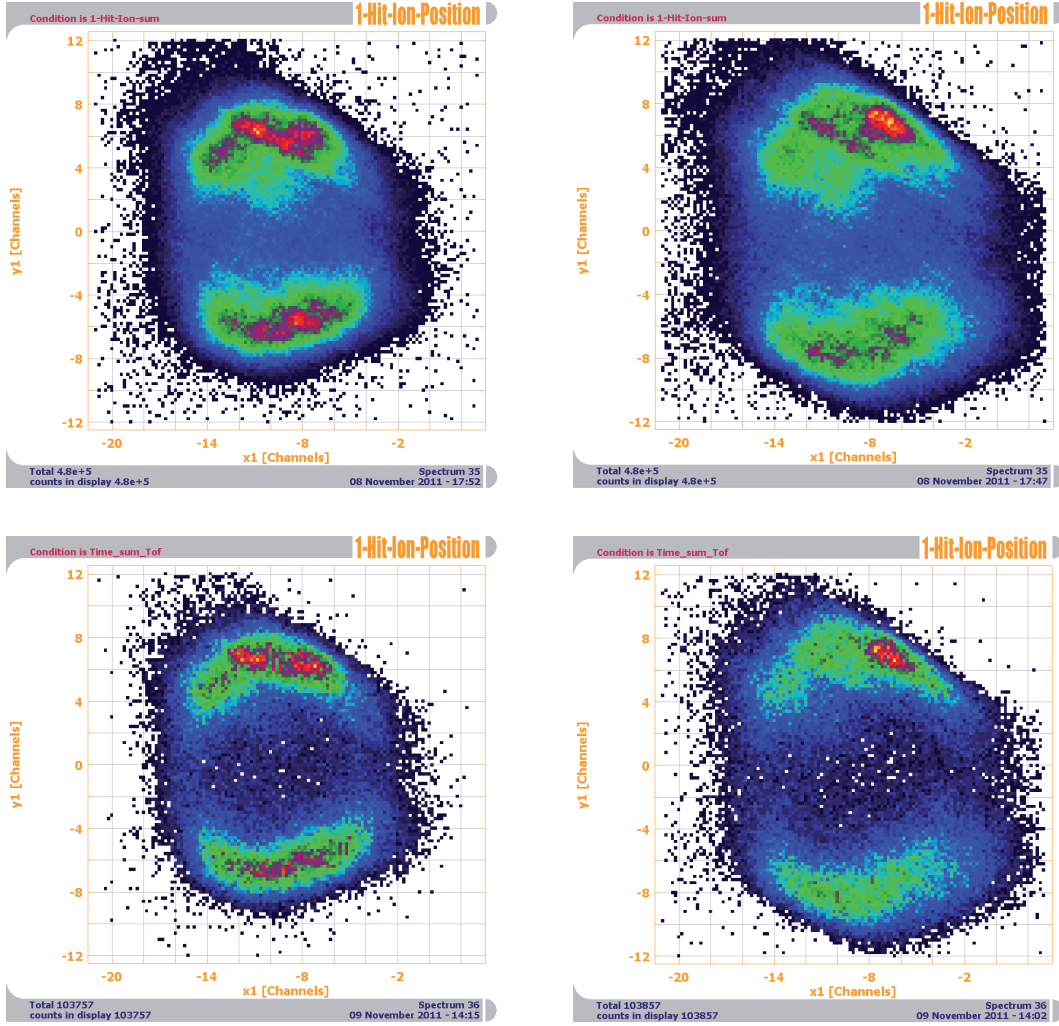


Figure 5.2: Measured spectra with the lens (left side) and without (right side). The top row shows the raw data, only a condition on the time sum of the delay line signals was imposed to suppress electronic noise. In the bottom row, a time-of-flight cut of 200 ns around the centre of the TOF distribution was applied, leaving mostly the events with high \vec{p}_\perp .

As a consequence of a short-circuit which occurred after bakeout, we were forced to set the zero point of the spectrometer voltage to an off-centre position. This led to the spectrometer acting like a cylinder lens, shrinking the detector picture along one axis. Because of the slotted spectrometer rings, there was also a vertical offset, since the extraction field was not top-bottom symmetric for the two rings in front of the aperture where the short-connection occurred. This explains the shape of the measured data,

5.1 Testing the spatial focusing

lens voltage	−2.72 V	−2.82 V	−2.92 V	−3.02 V	−3.12 V	−3.50 V	no lens
$\sigma_{\text{rise}} [\text{mm}]$	2.68	2.30	2.78	2.58	2.66	2.36	3.88
image size [mm]	16	16	16	15.8	15.6	15	18.4
$\sigma_{\text{rise}}/\text{size} [\times 10^{-2}]$	16.8	14.4	17.4	16.3	17.1	15.7	21.1
\vec{p}_{\perp} resolution [a.u.]	0.096	0.082	0.100	0.094	0.098	0.090	0.121

Table 5.1: Spectrometer performance with different lens settings. The image size was extracted from the whole detector picture without additional cuts. The sharpness parameter σ_{rise} was extracted from a fit as shown in figure 5.3.

but the focusing effect of the lens is still clearly visible. The previous best transverse momentum resolution of 0.08 a.u. (Schuricke et al. [39]) is matched with the lens despite these problems, while the configuration without the lens is reduced to 0.12 a.u.. The ultimate performance will have to be tested again after repairs and another bakeout of the experiment.

5.1.1 Comparison to Monte Carlo simulations

In order to directly compare the measured data to the simulations, the *Simion* program was not only run with the test patterns used to design the lens, but also with an ion recoil momentum distribution that corresponds to the experimental situation. The theoretical approach is being complicated by the fact that the atoms are ionised from a p -state ($2^2P_{3/2}$), leading to contributions from the s - and d -waves in the partial wave expansion. Without either experimental input or detailed wavefunctions, their amplitudes and relative phase cannot be determined.

Fortunately, Yang has shown in 1948 that in photon-atom interactions in the dipole approximation, for an unpolarised initial state of the atom, the angular correlation between the photon and an ejected particle is proportional to a linear combination of 1 and $\cos^2 \theta$ [41]. Here, θ is the angle between the polarisation vector of the incident photon and the outgoing electron. The main aspects of this result can be understood in an intuitive fashion: There is no term linear in $\cos \theta$, nor any odd powers of it, due to parity conservation in photoionisation; there are no higher even powers $\cos^{2n} \theta$ because the dipole approximation corresponds to the absorption of a single photon, changing the value l of the orbital angular momentum by at most one; there is no dependence on the azimuthal angle ϕ , as expected from the symmetry of the initial state. This result is most often parametrised in the form of the *anisotropy parameter* β :

5. MEASUREMENTS

$$\left(\frac{d\sigma}{d\Omega}\right)_{\text{unpol}} = \frac{\sigma}{4\pi}[1 + \beta P_2(\cos\theta)] \quad (5.2)$$

Here, σ is the total photoionisation cross section and P_2 is the second Legendre polynomial, i.e. $P_2(\cos\theta) = \frac{1}{2}(3\cos^2\theta - 1)$, giving the quadratic term in $\cos\theta$. Fitting the equation to the experimental data yields the value for β . It has to be noted that β is in general also energy-dependent. Nahar and Manson [42] give a general expression for β in the case of ionisation from the p -shell in dipole approximation:

$$\beta = 2 \frac{R^2 - 2R \cos \delta}{1 + 2R^2} \quad (5.3)$$

R is the ratio of the $p \rightarrow d$ and $p \rightarrow s$ dipole-matrix elements, while δ is the phase difference between those contributions. In the limits of pure s and pure d -waves, i.e. $R \rightarrow 0$ and $R \rightarrow \infty$, β takes values of 0 and 1 respectively. The maximum and minimum values for β are attained at equal mixing ($R = 1$) and lie between $+2$ and $-\frac{2}{3}$ depending on the relative phase. With a phase shift of π and equal mixing, one-photon ionisation from an *unpolarised* p -state can yield the same angular distribution as ionisation from an s -state: It looks like a pure p -wave which also has $\beta = 2$, even though it is actually a coherent superposition of s - and d -waves.

For the Monte Carlo detector pictures, the starting positions and momenta for 20 000 particles were randomly generated using *Mathematica*. The starting positions were picked according to a Gaussian distribution around the interaction point with $\sigma = 1$ mm. For the anisotropy parameter, a value of $\beta = 2$ was chosen, corresponding to a p -wave. Simion's *data recording* function was used to write the position and time of flight for every particle as it crosses the detector plane. This file was exported back to *Mathematica* where it was processed further. The Monte Carlo data was binned with the same binsize as the experimental data, and the same cut in the times of flight was applied, choosing a range of 200 ns around the centre of the TOF distribution. Figures 5.4 and 5.5 show the results with and without lens.

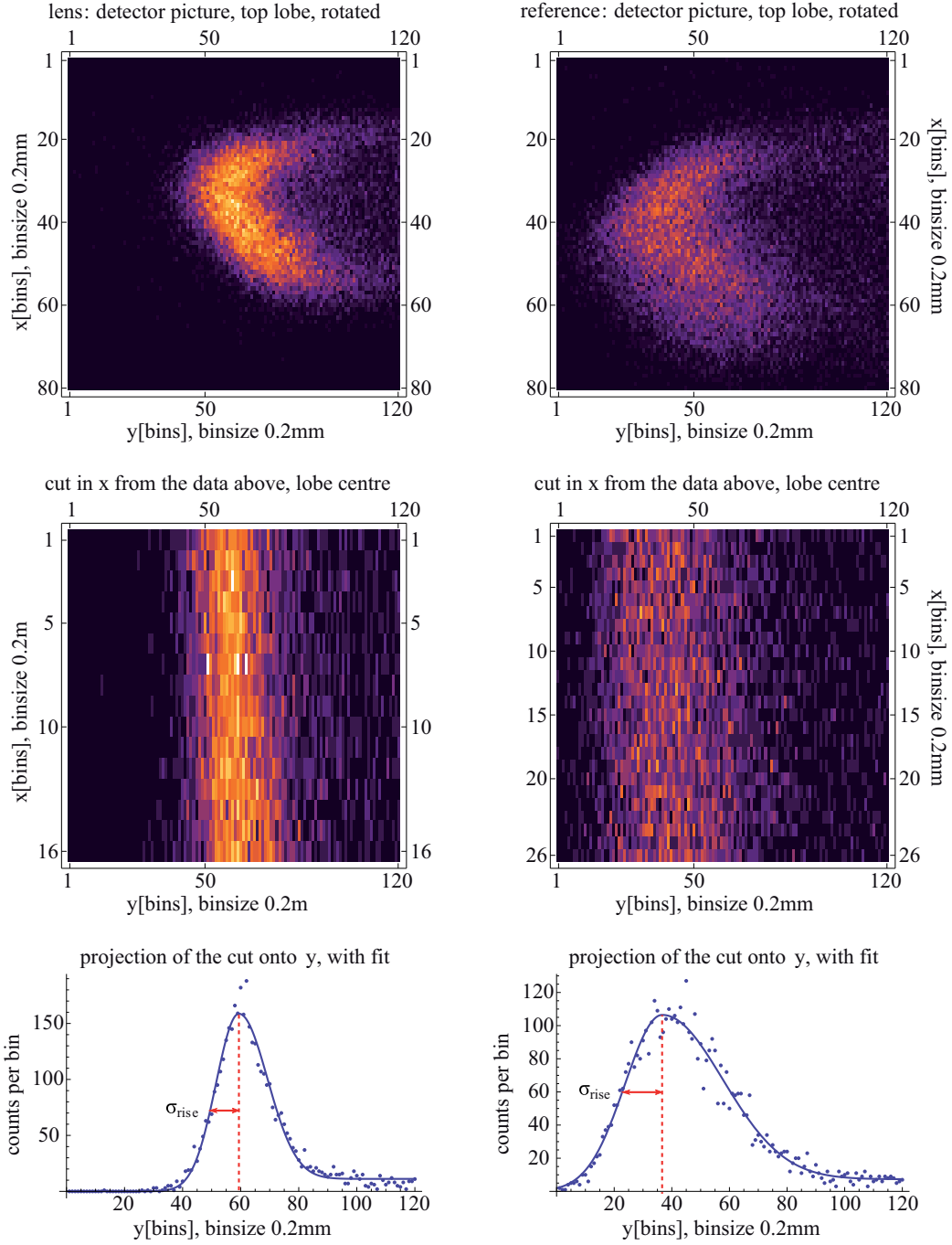


Figure 5.3: The left column contain the diagrams for a lens voltage of -2.82 V, the right one for the default configuration without a lens. In the top row, the part of the detector image containing the upper lobe is depicted, with a time-of-flight cut of 200 ns around the centre of the distribution already applied. The second row shows the x -cut that are the source for the fits in the bottom row. Two half-Gaussians with independent widths were employed to model the peak; the left width σ_{rise} gives the image resolution.

5. MEASUREMENTS

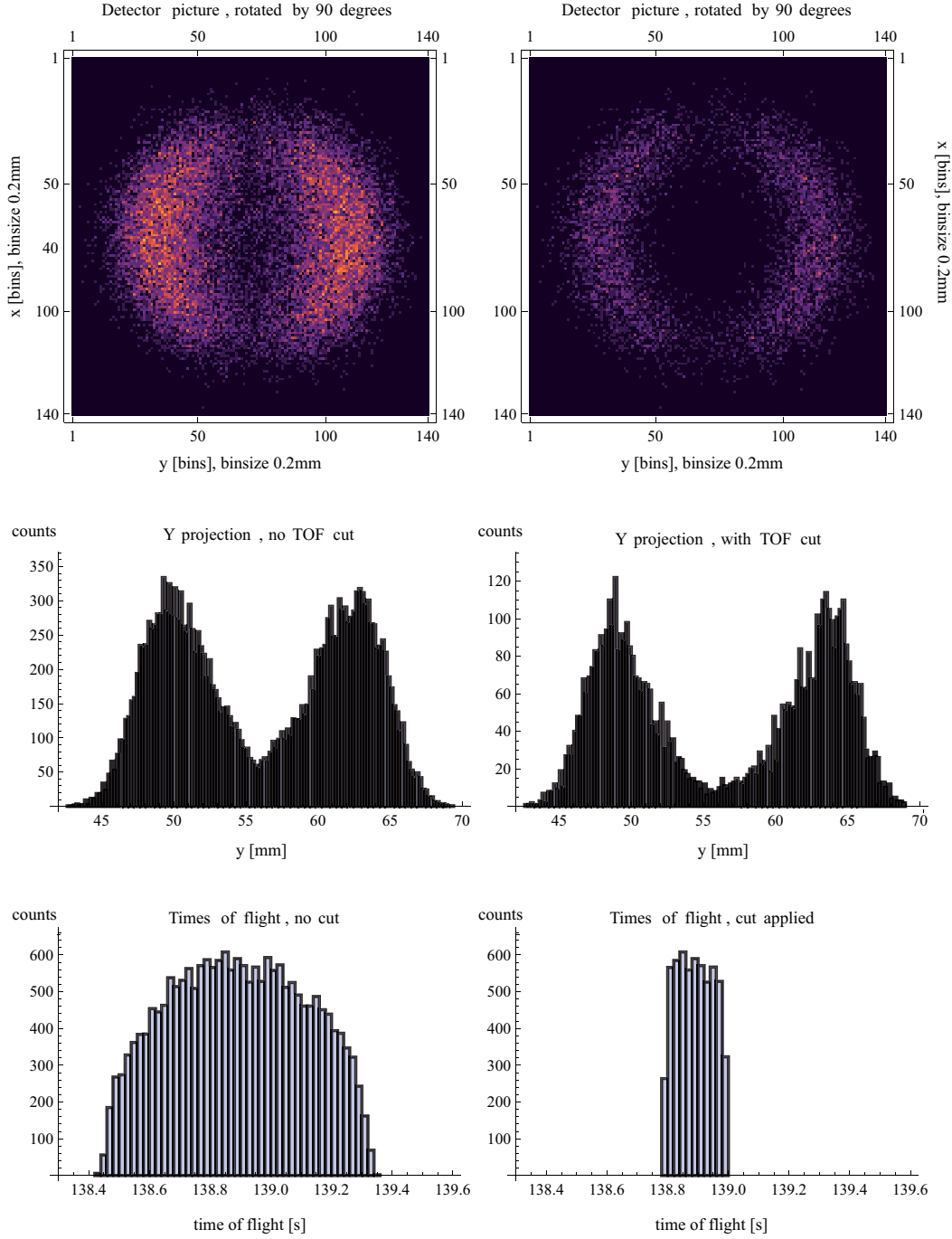


Figure 5.4: A full Monte Carlo simulation of a p -wave ion recoil momentum distribution. The ‘interaction volume’ was modelled by a Gaussian distribution with $\sigma = 1$ mm. Simion was used to determine the detector impact position and time of flight for all 20 000 random particles. The spectrometer voltage was set to 0.9 V on the electron side and 2.0 V on the ion side, giving a gradient of 0.1 V per ring or 0.08 V/cm. The drift length had the standard length for operation without a lens.

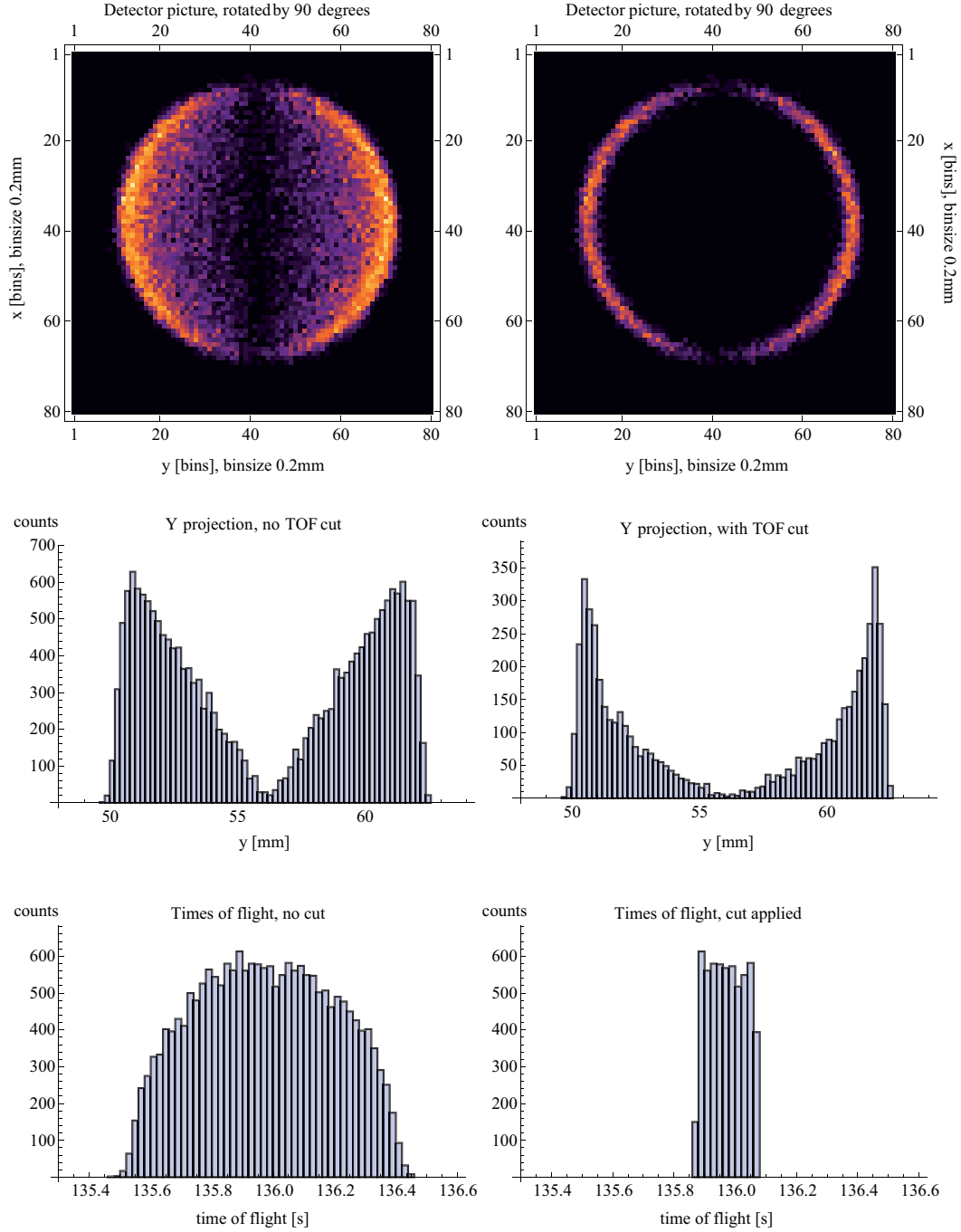


Figure 5.5: A full Monte Carlo simulation with the same set of particles as in the reference simulation without the lens. The spectrometer voltage was again set to 0.9 V on the electron side and 2.0 V on the ion side. The lens voltage was set to 4.5 V; the drift length was not changed for the lensing configuration, but no clear negative effect on the time of flight resolution is visible.

5. MEASUREMENTS

5.2 Retaining TOF-focusing

During the initial simulations (section 4.2.1), it became clear that the TOF-focusing condition of the drift length being twice the acceleration length does not hold when using an accelerating focusing lens. The 42 mm aperture was specifically made in order to restore perfect time focusing with two spectrometer rings added to the drift length. To verify this, the laser was turned by 90 degrees as a whole, so that the semi-major axis of the beam ellipsis and the polarisation of the laser are both aligned with the spectrometer axis. The time-of-flight distribution will now have a maximum at short and long times, corresponding to ions with maximum p_{\parallel} and therefore minimum \vec{p}_{\perp} . Three measurements were taken, first without the focusing lens, then with the lens but no change of the drift length, and finally with the lens and two spectrometer rings added to the drift length. The rising edge of the time-of-flight distribution had a width of about 18 ns for both the standard configuration and the lens with drift length correction. Without the correction, a marginally larger value of about 23 ns was obtained. This can probably be attributed to the fault in the spectrometer mentioned at the end of section 5.1 that smears out the time-of-flight distribution slightly, making it hard to see the effect of slightly missing the perfect TOF focusing condition. It is reassuring that the resolution is still very good despite these problems, highlighting the robustness of the Wiley-McLaren configuration.

5.3 Characterisation of the new MOT coils

To improve measurements with the electron part of the spectrometer, a new pair of MOT coils was built, as described in section 3.5.3. To quantify the enhancement, a number of characterisation measurements were performed. The goal was to compare the switch-off time of the new coils to the old ones, and to an air coil as well. The new coils were measured *in situ*, i.e. they were installed in the chamber. The old coils were measured outside, mounted on a holder to provide the same spacing as in the experiment. An air coil was made by removing the copper tube of one of the old coils from the rim and placing it on a non-metallic table. All three setups were driven by the IGBT-based MOT switch, and a current clamp was used to measure the coil current directly, for comparison with the magnetic field measurements. At first, it was tried to do these with a hall sensor; it had two modes of operation, ‘AC-mode’ and ‘DC-mode’. The

DC-mode can be used to measure the absolute value of the magnetic field, but it is too slow to properly measure the switch-off process. The AC-mode shows the fast drop of the field when the current is switched, but the relatively small contribution of the eddy currents for later times could not be measured satisfactorily, since the AC-measurement goes down to zero with its own time constant as well. When one is mainly interested in switching times, it is also possible to measure just the change of the magnetic flux inductively, instead of measuring the magnetic field directly. To do so, a small coil was wound from copper wire, and a matching resistor and capacitor were added. This gives the RLC circuit a small time constant as well as strong dampening, so that not only the rise of the magnetic flux through the coil at the beginning of the switch-off can be seen with good time resolution, but also the later falloff which we are interested in. This was verified by measuring the switching of the magnetic field of the air coil. In the absence of any conducting parts in the vicinity, the magnetic falloff should be as fast as the switching of the current. Figure 5.6 shows an oscilloscope screenshot of the air coil measurement; the current switching takes $80\text{ }\mu\text{s}$ according to the current clamp. The small measurement coil gives a symmetric peak for the switching, indicating that the timing is properly resolved. The full width of the peak is about $200\text{ }\mu\text{s}$, good enough for the following measurements. For the air coil, it can be concluded that the magnetic field is fully switched in a time between $80\text{--}200\text{ }\mu\text{s}$. As a comparison, *switching on* is displayed in figure 5.7.

For the old coils with a comparatively massive rim, the measured switching time is 2.7 ms . A similar time of around 3 ms has been reported by Schuricke [27] using a different method: electron spectra were taken at different delays after switching to determine how long it takes for the electron trajectories to be no longer perturbed by the residual magnetic field. The value and shape of the falloff depends slightly on the exact position and orientation of the coil within the spectrometer as well as on the threshold chosen to define ‘complete falloff’. The values stated here are ‘worst case’ values, and the threshold was chosen at $1/1000$ of the peak height. This cannot be translated into a magnetic field strength directly, but a comparison with the hall probe shows that the corresponding values are of the order of 0.5 Gauss , comparable to the Earth’s magnetic field. With the old coils, the falloff curve for the magnetic field clearly shows a ‘kink’ (see figure 5.8)—in some positions of the coil even an intermediate peak—caused by

5. MEASUREMENTS

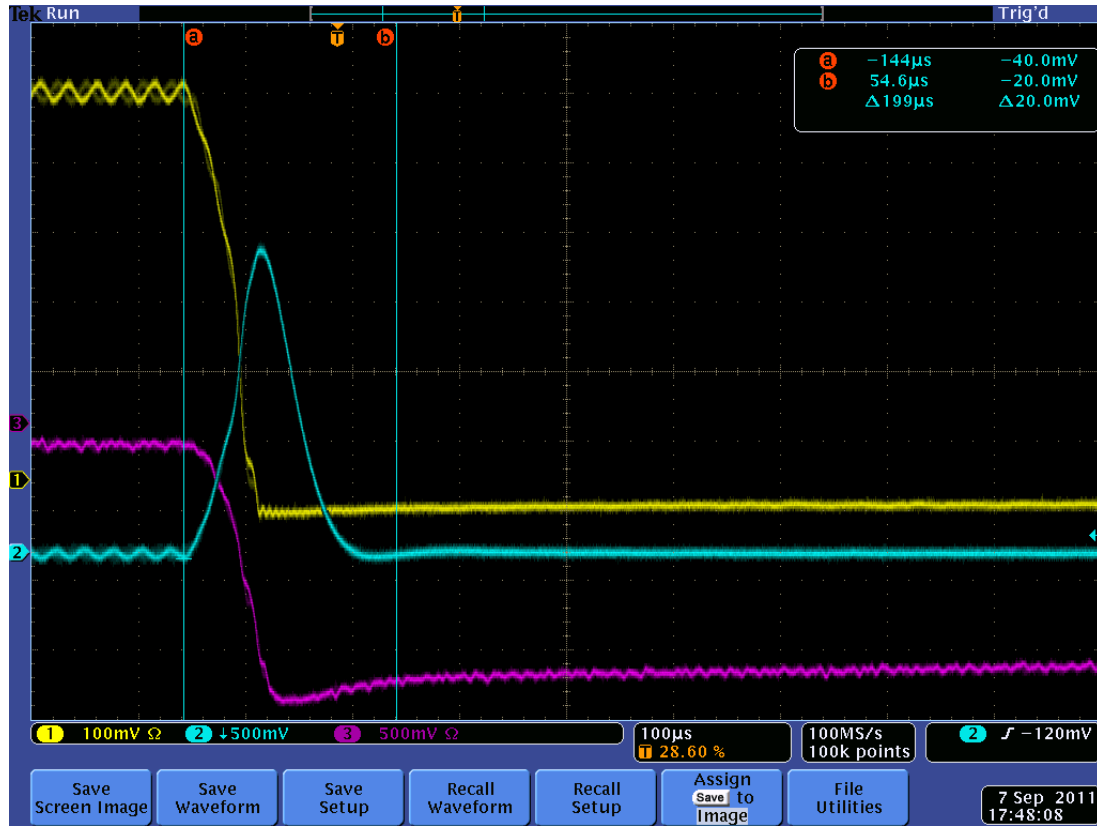


Figure 5.6: The switching-off process of the air coil. The yellow curve shows the current as measured with the current clamp, from 60 A to 0 (10 A/100 mV). The magenta curve is the magnetic field as measured by the hall probe, in arbitrary units. The cyan curve is the voltage induced in the measurement coil, taken with the oscilloscope port set to an impedance of 1 M Ω . The wiggles in the current are oscillations from the IGBT, which was adjusted to work with our old coils. When properly matched to the coils, there are no such disturbances.



Figure 5.7: The switching-on process of the air coil. The curves correspond to the same quantities as in figure 5.6. The ramping of the current by the IGBT is visible as a constant slope in the magnetic field and current measurements. The derivative of the magnetic flux, as measured by the small coil, shows as a plateau, as expected. The right side of the magenta curve shows the drift of the ‘AC-mode’-baseline for the hall probe; the measuring coil does not exhibit this behaviour. This measurement gives confidence in the coil data.

5. MEASUREMENTS

the eddy currents in the rim. The new coils, even with the disadvantage of being mounted inside the chamber with more material in the proximity, showed a falloff time of 0.9 ms. Surprisingly, this time rested the same when doing a measurement *without connecting the compensation coils*. Hall measurements verify that the magnetic field at the chamber walls is indeed strongly reduced (by about a factor of 100 at the MOT windows) when using the compensation coil, but the falloff time of the magnetic field inside the spectrometer does not seem to be affected much. In fact, no effect could be seen. It can be concluded that the improvement of the switching time by a factor of three is caused mainly by the new rim design. Ultimately, a further improvement by a factor of about five to ten could be possible with a rimless aircoil.



Figure 5.8: The switching-off process of the old coil. Yellow / magenta / cyan again correspond to current clamp / hall probe / measurement coil. In the coil data, the two parts of the switching process (directly switched current / eddy currents) and the ‘kink’ can be clearly seen. These effect cannot be seperated as well using the hall probe. Compared to the air coil in figure 5.6, the full falloff time of the magnetic field is about twenty times longer.

6

Results from FLASH 2010

In November and December 2010, our experiment embarked on a measurement campaign to the Free electron LASer in Hamburg, FLASH. The scientific goal was to study different mechanisms of multiphoton double ionisation in lithium for a comparison with both theory and earlier experiments on helium. The case of helium is by now understood quite well theoretically, so the differences between the two systems in theory and experiment can guide future developments. Owing to the high intensities available ($I \geq 10^{14} \text{W/cm}^2$) at rather high photon energies ($E_\gamma = 30\text{--}300 \text{ eV}$), FLASH enables for the first time studies on *non-linear* excitation and ionisation processes in this energy region. Of particular interest are reactions where the absorption of two or three photons gives rise to the correlated emission of several electrons from an atom. Measurements of non-sequential single and double ionisation at $E_\gamma = 50 \text{ eV}$ as well as sequential single and double ionisation at $E_\gamma = 59 \text{ eV}$ were made. Here, the latter process and its different reaction channels will be presented.

6.1 Introduction to photo double ionisation

As the name states, photo double ionisation (PDI) is a process where two electrons are removed from an atom by one photon. Thus, electron correlation is required. How can this be calculated theoretically and what would be a good intuitive picture to have of such an event?

Over the last twenty years, several mechanisms have been proposed and identified. The

strength of their contribution depends mainly on the photon energy. In the high energy regime, where the photon energy is well above the double ionisation threshold, it is now generally believed that initial state correlation is the dominant process for PDI. One electron absorbs the photon and is removed suddenly as it gains a high amount of energy; the correlated state of the other electron now relaxes onto the new ionic eigenstates. Its wave-function will have a certain overlap with the ionic continuum, which leads to it leaving the atom as well. This process has been dubbed *shakeoff*. It was observed in helium that the ratio between single and double ionisation cross section converges to a constant value of 1.67% in the high energy limit [43], a behaviour that had been theoretically predicted for shakeoff.

At lower energies, when the photon energy is just above the threshold for double ionisation, it has been proposed by Samson [44] that one electron absorbs the photon and then collides with the other electron, sharing the energy so that both can leave the atom. This had been called the *two-step-one* (TS1) process; it is clear that the e-e collision cross section diminishes strongly with rising electron energy ($\sigma \propto E^{-2}$) so that the TS1 mechanism becomes less efficient, and shakeoff eventually takes over.

Up to this point in the late 1990s, the details of the angular correlations of the electrons at different energies were not accessible experimentally, where only absolute cross sections or ratios thereof were measured. Theoretical consideration were the main drivers of progress so far, but could not be verified by experimental data. With the advent of COLd Target Recoil Ion Momentum Spectroscopy (COLTRIMS), the full kinematic information on the ion recoil momentum could be determined. This is equivalent to measuring the sum momentum of the two outgoing electrons, which gives insight into the energy sharing and angular correlation between them.

6.2 Multiphoton ionisation

The next level of complexity was to widen the scope from one-photon-few-electron dynamics to few-photon-few-electron processes, i.e. multiphoton double and triple ionisation. The two main categories of multiphoton ionisation mechanisms are sequential and non-sequential processes. In a sequential process, the photon energy is high enough to ionise an atom step by step, each photon ejecting one electron. However, ‘nearly sequential’ processes are still possible even when the photon energy is not sufficient

for direct ionisation. If it has the right energy, the first photon can resonantly excite the atom into a state with a lifetime of the order of the pulse length or greater. A second photon is then absorbed by the excited atom, causing the ejection of two photoelectrons in a PDI process. The large possible time delay between the two absorption events makes it possible to treat the ionisation as two quasi-independent sequential processes, first excitation and then PDI. This makes the calculations comparatively straightforward, but by no means simple in the case of lithium.

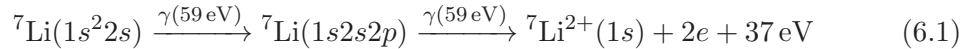
In a non-sequential process on the other hand, there is no long-lived intermediate excited state, so the two photons have to be absorbed simultaneously. This leads to a different scaling of the two processes with the laser intensity:

In the sequential process, each step is linear in intensity when the atomic population is mainly in the ground state, so a two-photon process would scale with the intensity squared. However, if the intensity is high or the transition cross-section for the first step is large, the intermediate state can become macroscopically populated or even saturated. At this point, the intensity scaling will become linear, as it is only the second step now that limits the two-step process.

For a non-sequential process on the other hand, the scaling is always with the intensity squared. Only with very intense and preferably short pulses do they become significant and can be observed. The data analysis for these measurements is still ongoing, as are theoretical calculations.

6.3 Preliminary results for sequential double ionisation

One of the series of measurements was quasi-sequential double ionisation via the $2p$ -state using resonant 59 eV photons:



Two such photons have a combined energy of 118 eV, while the sum of the first and second ionisation potentials of lithium is 81 eV (see table 2.1), yielding an excess energy of about 37 eV that is shared by the two outgoing electrons. In the second step (DPI), the double ionisation has to be mediated by electron correlation.

6. RESULTS FROM FLASH 2010

Experimentally, we have observed only the recoil ion momentum, which is the opposite of the sum momentum of the two electrons due to momentum conservation. A certain recoil momentum can be reached by different combinations of the angle between the electrons and their energy sharing, so it is not possible to completely disentangle these two parameters. Nevertheless, the overall shape of the recoil ion momentum distribution is characteristic for each process and can be compared with theory.

Only for the extremes of the ion recoil momentum distribution the relative angles of the electrons are fixed. For equal energy sharing and back-to-back emission of the electrons, the recoil ion momentum distribution is peaked at 0 a.u. If both electrons emitted in the same direction with equal energy sharing, the maximum possible recoil ion momentum of in this case $2 \times \sqrt{2 \cdot 18.5 \text{ eV} / 27.21 \text{ eV}} = 2.33 \text{ a.u.}$ is reached.

The final state ${}^7\text{Li}^{2+}(1s)$ can also be reached via a three-photon process, where the $2s$ and $2p$ electrons from the ${}^7\text{Li}(1s2s2p)$ intermediate state independently absorb one photon each. The additional energy of 59 eV leads to higher ion recoil momenta up to a theoretical maximum of 4.16 a.u. Figure 6.1 shows the level scheme diagrams for both processes.

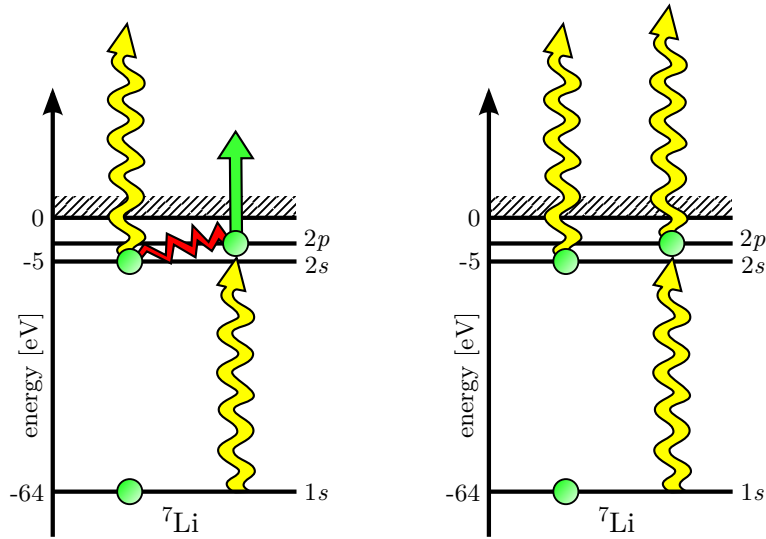


Figure 6.1: The 2γ (left) and 3γ (right) processes for double ionisation of ${}^7\text{Li}$ at $E_\gamma = 59 \text{ eV}$. The first step in both diagrams is the excitation from $1s$ to $2p$; in the 3γ process, the two following absorptions can happen in any order.

In order to record the signal of the reaction of interest, it was necessary to suppress

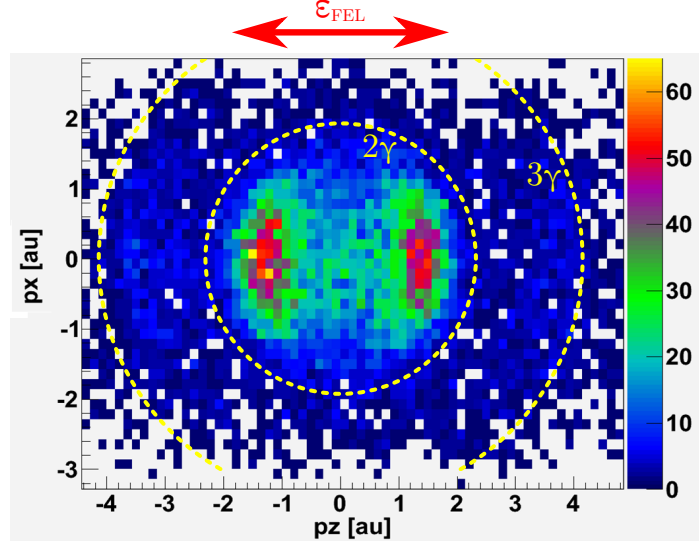


Figure 6.2: Data taken at FLASH with $E_\gamma = 59$ eV and special detector settings, suppressing the background from single ionisation events. The longitudinal recoil ion momentum p_{\parallel} is plotted on the horizontal axis, the x-component of the transverse recoil ion momentum on the vertical axis. The FEL pulse was linearly polarised along the spectrometer axis, giving the two peaks in p_{\parallel} . The dashed yellow circles show the possible maximum recoil ion momentum for two and three photon double ionisation.

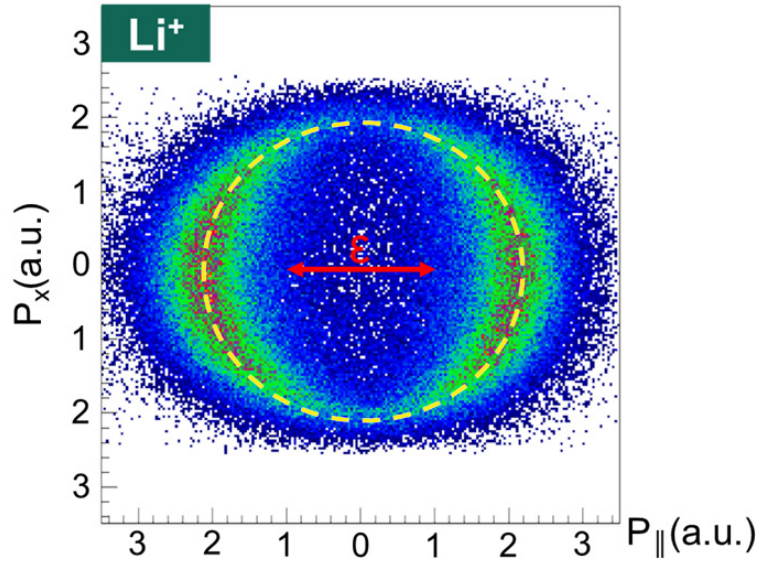


Figure 6.3: Longitudinal recoil ion momentum plotted against transverse recoil ion momentum in X-direction for two photon single ionisation of ^7Li at $E_\gamma = 59$ eV. The dashed yellow circle corresponds to the excess energy of 1.98 a.u.

6. RESULTS FROM FLASH 2010

the high number of single ionisation events from the lithium target as well as the residual gas. Instead of only making a TOF selection for ${}^7\text{Li}^{2+}$ after the fact, which would not have helped against the limit of the total ion flux that the MCP can handle ($\approx 20\,000$ hits/s), the MCP was operated in a different mode compared to normal ion detection. Usually, the MCP is at a relative voltage of about -2500 V to the mesh in front of it, which is at the potential of the drift tube. Once the ions pass through the mesh, they are accelerated onto the MCP, which gives them the needed kinetic energy to trigger an electron avalanche. For these measurements, the voltage difference between mesh and MCP was lowered to only about -100 V ; normal singly ionised $\text{Li}^+(1s^2)$ has a very low detection efficiency at these settings [45]. The ${}^7\text{Li}^{2+}(1s)$ ions do have an empty spot in their K -shell though, so an energy corresponding to the second ionisation potential of 75.64 eV can be released during electronic recombination at the surface of the MCP. This is sufficient to start the electron avalanche and generate a signal. Using this technique, a very good signal-to-noise ratio is achieved; the ‘background’, namely the ${}^7\text{Li}^+(1s^2)$ and residual gas ions are suppressed by a factor of about 10^3 . Our experiment was operated as a pure COLTRIMS setup for these measurements (only recording recoil ion momenta) because no similar technique exists to filter out all the electrons from the background events. An experimentally measured spectrum with these detector settings and a photon energy of 59 eV is depicted in figure 6.2. Two distinct peaks in the longitudinal recoil ion momentum at around $\pm 1.4\text{ a.u.}$ are visible, corresponding to the two photon process. The weaker signal around $\pm 3.6\text{ a.u.}$ corresponding to the three photon process is also aligned along the polarisation axis.

6.3.1 A look a single ionisation

Instead of being doubly ionised by a PDI process, the intermediate state ${}^7\text{Li}(1s2s2p)$ often just undergoes single ionisation by another photon. What makes looking at this process interesting is that the linearly polarised FLASH pulse only populates the ($m_l = 0$)-substates (singlet and triplet) of the $2p$ -shell, leading to an aligned initial state for the absorption of the second photon. This implies that equation (5.2) is not applicable here, meaning that the angular distribution can possibly not be described by the beta parameter alone. Figure 6.3 shows our measurement of two photon single ionisation at $E_\gamma = 59\text{ eV}$, generated from the same dataset as the double ionisation by

applying a time-of-flight selection for singly charged lithium ions. The reason we are able to detect them with a reasonable efficiency is that they have a hole in the K -shell, enabling detection with the special MCP settings. The possible reactions for the second photon are:

$${}^7\text{Li}(1s2s2p) \xrightarrow{\gamma(59\text{ eV})} \left\{ {}^7\text{Li}^+(1s2s), {}^7\text{Li}^+(1s2p) \right\} + e + \text{energy} \quad (6.2)$$

The ${}^7\text{Li}^+(1s2p)$ final state cannot be observed, since it has a fast dipole-allowed decay channel to ${}^7\text{Li}^+(1s^2)$, after which it will not be detected. The metastable ${}^7\text{Li}^+(1s2s)$ -state is observable, i.e. its lifetime is long enough to reach the detector (≈ 1 min [46]). The electron excess energy is given by:

$$\begin{aligned} E(e) &= 2 \cdot 59\text{ eV} - \text{IP}_{\text{Li}} - \Delta E({}^7\text{Li}^+(1s2s), {}^7\text{Li}^+(1s^2)) \\ &= 118\text{ eV} - 5.4\text{ eV} \begin{cases} -60.9\text{ eV} & = 53.6\text{ eV} = 1.98\text{ a.u. (singlet)} \\ -59.0\text{ eV} & = 51.7\text{ eV} = 1.95\text{ a.u. (triplet)} \end{cases} \end{aligned} \quad (6.3)$$

Fitting the angular distribution of the two-photon single ionisation with the anisotropy parameter β indeed cannot describe the single ionisation data, confirming that the initial state for the absorption of the second photon was not isotropic. As figure 6.4 shows, a good fit can be achieved by introducing the parameter β_4 , extending equation (5.2) by the next even Legendre polynomial P_4 . In multiphoton processes of still higher order, more β -factors would have to be introduced [41]. In this context, β is usually renamed β_2 :

$$\begin{aligned} \left(\frac{d\sigma}{d\Omega} \right) &= \frac{\sigma}{4\pi} [1 + \beta_2 P_2(\cos \theta) + \beta_4 P_4(\cos \theta)] \\ &= \frac{\sigma}{4\pi} [1 + \frac{\beta_2}{2} (3 \cos^2 \theta - 1) + \frac{\beta_4}{8} (35 \cos^4 \theta - 30 \cos^2 \theta + 3)] \end{aligned} \quad (6.4)$$

6.4 Comparison with theory

A. Kheifets has performed calculations on the two-photon quasi-sequential double ionisation process at 59 eV in the framework of the time-dependent close coupling (TDCC) formalism [47]. Figure 6.5 shows the overall result of a new TDCC calculation [48], as well as the two constituent contributions from the singlet and triplet $2p$ initial state.

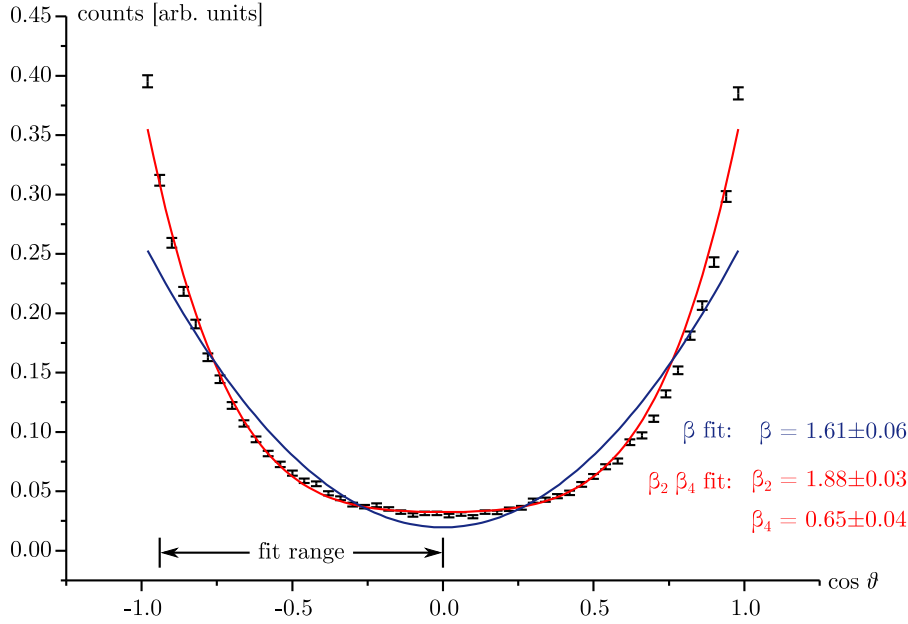


Figure 6.4: Data from two photon single ionisation at 59 eV (figure 6.3) has been binned according to the angle θ between the polarisation axis of the FEL and the recoil ion momentum. Fits show that the anisotropy parameter β alone is not sufficient to describe the data.

The combination of both describes the data reasonably well, reproducing the two outer lobes as well as a peak in the centre; the dominant contribution seems to stem from the singlet initial state. In our experimental data (figure 6.2), the centre of the momentum distribution looks more evenly filled and less peaked around zero, but the limited resolution and statistics do not allow a conclusive answer yet. The position of the intensity maximum in the lobes lies at higher momentum values in the experiment (≈ 1.5 a.u.) compared to the theory (≈ 0.9 a.u.), which is not yet understood. On the theoretical side, unequal energy sharing or big relative angles between the electrons could be overpronounced. Experimentally, the presence of all the singly charged lithium ions that are not detected could lead to space charge effects.

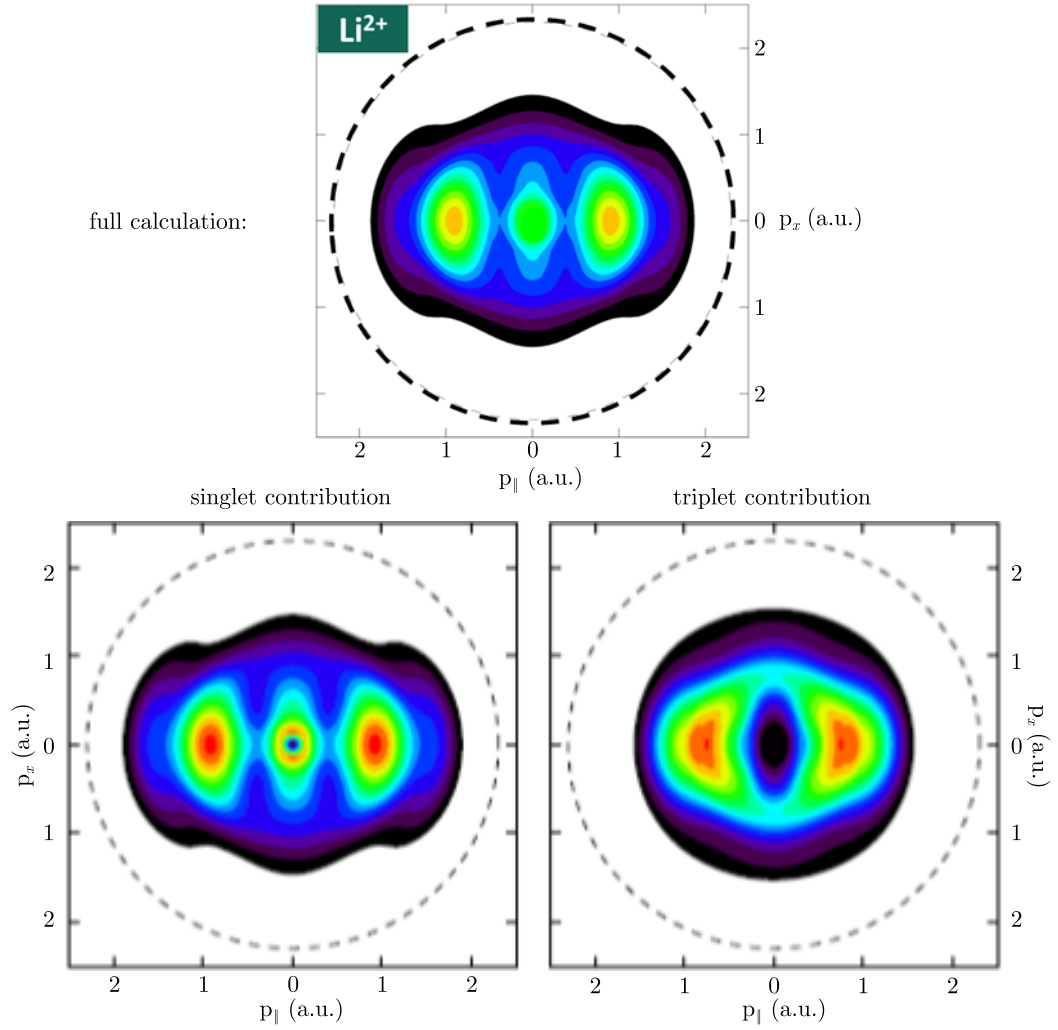


Figure 6.5: A numerical simulation of the PDI step in the quasi-sequential double ionisation of lithium by A. Keifets [48]. Both the singlet and triplet configuration of the intermediate ${}^7\text{Li}(1s2s2p)$ -state have to be taken into account.

Conclusion and outlook

The aim of this work was to improve a reaction microscope for future studies on electron impact ionisation and multiphoton processes. The experiment combines a lithium magneto-optical trap and a multi-particle imaging spectrometer, two state-of-the-art experimental techniques in experimental atomic physics. While the setup has been able to deliver recoil ion momentum measurements with excellent resolution when using a strongly focused projectile laser, two obstacles for further experiments had been identified.

Firstly, the switching time of the MOT magnetic field was severely prolonged by eddy currents, hampering measurements of the electrons. The long waiting time leads to an extremely low duty cycle and a dilute target. Though possible in principle, such measurements were therefore impractical under the time constraints of a beam time. In this work, a new pair of MOT coils has been built and characterised, yielding a reduction of the switching time by a factor of three. The source of the eddy currents has been identified in the coil rim, pointing out the direction for further improvements or upgrades of other experiments. This better duty cycle will enable coincident observation of ions and electrons at the free electron laser in Hamburg. Providing the additional information given by ion-electron coincidences will enable a better understanding of few-photon few-electron quantum dynamics.

Planned experiments making use of the multi-hit electron detection capabilities are fully differential measurements of double and triple ionisation, investigating the differ-

7. CONCLUSION AND OUTLOOK

ent sequential and non-sequential reaction pathways. A particularly interesting issue is the initial state dependence of the breakup geometry close to the threshold. Calculations by Emmanouilidou et al. [49] indicate that for three-electron breakup, apart from the symmetric triangular configuration that is expected from Wannier threshold treatment [50, 51], a breakup of lower symmetry in the form of a T-shape can also occur. According to Emmanouilidou et al., the T-shape should be prominent for one photon triple ionisation of ground state lithium, but this is yet to be experimentally confirmed. The T-shape fragmentation geometry is also predicted for electron impact double ionisation, i.e. $(e,3e)$ on ${}^7\text{Li}(1s^22s)$. Performing these experiments would therefore be very promising to either confirm or refute this theory.

Another interesting type of experiment uses additional lasers to excite or align the initial state. One such idea is to realise laser-switching between sequential and non-sequential K -shell double ionisation at FLASH. Laser excitation of lithium from $2s$ to $2p$ lowers the threshold energy for sequential double ionisation (SDI) from 108.4 eV for ${}^7\text{Li}(1s2s^2)$ to 106.1 eV for ${}^7\text{Li}(1s2s2p)$. Setting the photon energy of the FEL between these two values, the pumping laser can then be used enable or disable SDI. The direct comparison of above and below SDI threshold spectra would provide detailed information on strongly debated issues in theory, namely *virtual sequential ionisation* [52, 53] and the *total cross section slope* in the vicinity of the non-sequential double ionisation threshold [54].

The second obstacle tackled in this thesis was the reduced recoil ion momentum resolution when using an extended projectile beam, due to the size of the reaction volume. While it had already been envisioned to operate the spectrometer in a 3D-focusing configuration in the original design of the experiment [20], the idea was suspended after the initial attempts failed. In this thesis, a cautious approach was taken, combining thorough simulations with experimental flexibility, allowing to revert to the standard configuration at any time. Monte Carlo simulations and corresponding measurements with a UV laser confirm the successful implementation of spatial focusing, enabling a higher recoil ion momentum resolution for extended reaction volumes. This will enable precise measurements of electron impact ionisation. Measurements at a synchrotron source such as PETRA III would equally profit from spatial focusing of the ions. While

the brilliance and peak intensities are lower than at FLASH, small pulses at a rate in the megahertz range provide clean measurements of individual ionisation events, since the expected event rate per shot would be significantly below one. The electron momenta recorded could be assigned to a single recoil ion, which is not possible with the many events from each pulse at an FEL. For studies of sequential processes which do not require extreme intensities, synchrotrons do therefore have advantages over FELs. With focused FEL beams, the beam waist is small, but the Rayleigh length of the focus is usually on the order of centimetres. The electrostatic lens will therefore improve the recoil ion momentum resolution along the projectile beam axis. In general, relaxing the need for a focused projectile for reasons of momentum resolution also helps avoiding target depletion. In the future, strongly focused beams will only be needed when the physical processes of interest require high intensities.

7. CONCLUSION AND OUTLOOK

References

- [1] R. Moshhammer, B. Feuerstein, W. Schmitt, A. Dorn, C. D. Schröter, J. Ullrich, H. Rottke, C. Trump, M. Wittmann, G. Korn, K. Hoffmann, and W. Sandner. Momentum distributions of Ne^{n+} ions created by an intense ultrashort laser pulse. *Phys. Rev. Lett.*, 84: 447–450, Jan 2000. 1
- [2] Th. Weber, M. Weckenbrock, A. Staudte, L. Spielberger, O. Jagutzki, V. Mergel, F. Afaneh, G. Urbasch, M. Vollmer, H. Giessen, and R. Dörner. Recoil-ion momentum distributions for single and double ionization of helium in strong laser fields. *Phys. Rev. Lett.*, 84: 443–446, Jan 2000. 1
- [3] A. Rudenko, K. Zrost, B. Feuerstein, V. L. B. de Jesus, C. D. Schröter, R. Moshhammer, and J. Ullrich. Correlated multielectron dynamics in ultrafast laser pulse interactions with atoms. *Phys. Rev. Lett.*, 93:253001, Dec 2004. 1
- [4] M. Kurka, J. Feist, D. A. Horner, A. Rudenko, Y. H. Jiang, K. U. Kühnel, L. Foucar, T. N. Rescigno, C. W. McCurdy, R. Pazourek, S. Nagele, M. Schulz, O. Herrwerth, M. Lezius, M. F. Kling, M. Schffler, A. Belkacem, S. Dsterer, R. Treusch, B. I. Schneider, L. A. Collins, J. Burgdörfer, C. D. Schrter, R. Moshhammer, and J. Ullrich. Differential cross sections for non-sequential double ionization of He by 52 eV photons from the Free Electron Laser in Hamburg, FLASH. *New Journal of Physics*, 12:073035, 2010. 2
- [5] A. Rudenko, Y. H. Jiang, M. Kurka, K. U. Khnel, L. Foucar, O. Herrwerth, M. Lezius, M. F. Kling, C. D. Schrter, R. Moshhammer, and J. Ullrich. Exploring few-photon, few-electron reactions at FLASH: from ion yield and momentum measurements to time-resolved and kinematically complete experiments. *Journal of Physics B*, 43:194004, 2010. 2
- [6] L. Strüder, S. Epp, D. Rolles, R. Hartmann, P. Holl, G. Lutz, H. Soltau, R. Eckart, C. Reich, K. Heinzinger, C. Thamm, A. Rudenko, F. Krasniqi, K. U. Khnel, C. Bauer, C. D. Schrter, R. Moshhammer, S. Techert, D. Miessner, M. Porro, O. Hälker, N. Meidinger, N. Kimmel, R. Andritschke, F. Schopper, G. Weidenspointner, A. Ziegler, D. Pietschner, S. Herrmann, U. Pietsch, A. Walenta, W. Leitenberger, C. Bostedt, T. Möller, D. Rupp, M. Adolph, H. Graafsma, H. Hirsemann, K. Gärtner, R. Richter, L. Foucar, R. L. Shoeman, I. Schlichting, and J. Ullrich. Large-format, high-speed, X-ray pnCCDs combined with

REFERENCES

- electron and ion imaging spectrometers in a multipurpose chamber for experiments at 4th generation light sources. *Nuclear Instruments and Methods in Physics Research Section A: Accelerators, Spectrometers, Detectors and Associated Equipment*, 614(3):483 – 496, 2010. 2
- [7] R. Frisch. Experimenteller Nachweis des Einsteinschen Strahlungsrückstoßes. *Zeitschrift für Physik*, 86:42–48, 1933. 5
- [8] D. J. Wineland, R. E. Drullinger, and F. L. Walls. Radiation-pressure cooling of bound resonant absorbers. *Phys. Rev. Lett.*, 40:1639–1642, Jun 1978. 5
- [9] W. Neuhauser, M. Hohenstatt, P. Toschek, and H. Dehmelt. Optical-sideband cooling of visible atom cloud confined in parabolic well. *Phys. Rev. Lett.*, 41:233–236, Jul 1978. 5
- [10] R. Schieder, H. Walther, and L. Wöste. Atomic beam deflection by the light of a tunable dye laser. *Optics Communications*, 5:337–340, 1972. 5
- [11] W. D. Phillips and H. J. Metcalf. Laser deceleration of an atomic beam. *Phys. Rev. Lett.*, 48:596–599, Mar 1982. 5
- [12] Steven Chu, L. Hollberg, J. E. Bjorkholm, A. Cable, and A. Ashkin. Three-dimensional viscous confinement and cooling of atoms by resonance radiation pressure. *Phys. Rev. Lett.*, 55:48–51, Jul 1985. 5, 8
- [13] Steven Chu, J. E. Bjorkholm, A. Ashkin, and A. Cable. Experimental observation of optically trapped atoms. *Phys. Rev. Lett.*, 57:314–317, Jul 1986. 5
- [14] E. L. Raab, M. Prentiss, A. Cable, Steven Chu, and D. E. Pritchard. Trapping of neutral sodium atoms with radiation pressure. *Phys. Rev. Lett.*, 59:2631–2634, Dec 1987. 5, 10
- [15] H. J. Metcalf and P. Van der Straten. *Laser Cooling and Trapping*. Springer-Verlag, 1999. 5, 6, 8, 9
- [16] M. L. Citron, H. R. Gray, C. W. Gabel, and C. R. Stroud. Experimental study of power broadening in a two-level atom. *Phys. Rev. A*, 16:1507–1512, Oct 1977. 7
- [17] United States National Institute of Standards and Technology. Atomic Weights and Isotopic Compositions. URL <http://www.nist.gov/pml/data/>. 10
- [18] R. B. Firestone. Exploring the Table of Isotopes. URL <http://ie.lbl.gov/education/isotopes.htm>. 10
- [19] W.M. Haynes. *CRC Handbook of Chemistry and Physics*, 92nd Edition. Taylor and Francis, 2011. 10
- [20] J. Steinmann. *Multiphoton ionization of laser cooled lithium*. PhD thesis, Universität Heidelberg, 2007. 11, 32, 74

-
- [21] M. Berglund and M. E. Wieser. Isotopic compositions of the elements 2009 (IUPAC Technical Report). *Pure Appl. Chem.*, 83:397–410, Jan 2011. 11
- [22] Christopher J. Foot. *Atomic Physics (Oxford Master Series in Atomic, Optical and Laser Physics)*. Oxford University Press, USA, 2005. 12, 14, 30
- [23] J. Ullrich, R. Moshhammer, R. Dörner, O. Jagutzki, V. Mergel, H. Schmidt-Böcking, and L. Spielberger. Recoil-ion momentum spectroscopy. *J. Phys. B*, 30:2917–2974, July 1997. 15
- [24] J. Ullrich, R. Moshhammer, A. Dorn, R. Dörner, L. P. H. Schmidt, and H. Schmidt-Böcking. Recoil-ion and electron momentum spectroscopy: reaction-microscopes. *Rep. Prog. Phys.*, 66:1463–1545, Sept 2003. 15
- [25] W. C. Wiley and I. H. McLaren. Time-of-flight mass spectrometer with improved resolution. *Review of Scientific Instruments*, 26(12):1150–1157, 1955. 18
- [26] O. Jagutzki, A. Cerezo, A. Czasch, R. Dorner, M. Hattas, Min Huang, V. Mergel, U. Spillmann, K. Ullmann-Pfleger, T. Weber, H. Schmidt-Böcking, and G.D.W. Smith. Multiple hit readout of a microchannel plate detector with a three-layer delay-line anode. *Nuclear Science, IEEE Transactions on*, 49:2477–2483, Oct 2002. 20
- [27] M. Schuricke. *Multiphoton Ionization of Lithium*. Diplomarbeit, Universität Heidelberg, 2008. 23, 24, 59
- [28] J. M. J. Madey. Stimulated emission of bremsstrahlung in a periodic magnetic field. *Journal of Applied Physics*, 42:1906–1913, 1971. 27
- [29] A. A. Zholents and G. Penn. Obtaining attosecond x-ray pulses using a self-amplified spontaneous emission free electron laser. *Phys. Rev. ST Accel. Beams*, 8:050704, May 2005. 28
- [30] R. Hubele. *Implementation of an Optical Dipole Trap for Lithium*. Diplomarbeit, Universität Heidelberg, 2009. 32
- [31] M. Schöffler. *Grundzustandskorrelationen und dynamische Prozesse untersucht in Ion-Helium-Stößen*. PhD thesis, Universität Frankfurt, 2006. 35
- [32] H. Busch. Über die Wirkungsweise der Konzentrierungsspule bei der Braunschen Röhre. *Archiv für Elektrotechnik*, 18:583–594, 1927. 36
- [33] E. Brüche. Die Grundlagen der angewandten geometrischen Elektronenoptik. *Archiv für Elektrotechnik*, 29:79–107, 1935. 36
- [34] A. L. Septier. *Aberration sphérique de quelques lentilles électrostatiques à symétrie de révolution pour des faisceaux de grande ouverture*. CERN, Geneva, 1960. 37

REFERENCES

- [35] D. A. Dahl. Simion for the personal computer in reflection. *International Journal of Mass Spectrometry*, 200:3–25, 2000. 37
- [36] D.C. McGilvery. Proceedings of the 46th ASMS Conference on Mass Spectrometry and Allied Topics (May 31–June 4, 1998, Orlando, Florida). 37
- [37] G. Zhu, M. Schuricke, J. Steinmann, J. Albrecht, J. Ullrich, I. Ben-Itzhak, T. J. M. Zouros, J. Colgan, M. S. Pindzola, and A. Dorn. Controlling two-electron threshold dynamics in double photoionization of lithium by initial-state preparation. *Phys. Rev. Lett.*, page 103008, Sep 2009. 49
- [38] L. J. Radziemski, R. Engleman, and J. W. Brault. Fourier-transform-spectroscopy measurements in the spectra of neutral lithium, ^6Li and ^7Li (li i). *Phys. Rev. A*, 52:4462–4470, Dec 1995. 50
- [39] M. Schuricke, Ganjun Zhu, J. Steinmann, K. Simeonidis, Igor Ivanov, A. Kheifets, A. N. Grum-Grzhimailo, K. Bartschat, A. Dorn, and J. Ullrich. Strong-field ionization of lithium. *Phys. Rev. A*, 83:023413, Feb 2011. 50, 53
- [40] N. Amin, S. Mahmood, M. Saleem, M. A. Kalyar, and M. A. Baig. Photoionization cross-section measurements from the $2p$, $3d$ and $3s$ excited states of lithium. *The European Physical Journal D*, 40:331–337, Aug 2006. 50
- [41] C. N. Yang. On the angular distribution in nuclear reactions and coincidence measurements. *Phys. Rev.*, 74:764–772, Oct 1948. 53, 69
- [42] S. N. Nahar and S. T. Manson. Photoelectron angular distribution of the excited $2p^23p^2$ state of atomic nitrogen. *Phys. Rev. A*, 40:5017–5019, Nov 1989. 54
- [43] L. Spielberger, O. Jagutzki, R. Dörner, J. Ullrich, U. Meyer, V. Mergel, M. Unverzagt, M. Damrau, T. Vogt, I. Ali, Kh. Khayyat, D. Bahr, H. G. Schmidt, R. Frahm, and H. Schmidt-Böcking. Separation of photoabsorption and compton scattering contribution to the single and double ionization. *Phys. Rev. Lett.*, 74:4615–4618, Jun 1995. 64
- [44] James A. R. Samson. Proportionality of electron-impact ionization to double photoionization. *Phys. Rev. Lett.*, 65:2861–2864, Dec 1990. 64
- [45] M. Krems, J. Zirbel, M. Thomason, and R. D. DuBois. Channel electron multiplier and channelplate efficiencies for detecting positive ions. *Review of Scientific Instruments*, 76:093305, 2005. 68
- [46] R. D. Knight and M. H. Prior. Radiative lifetime of metastable 2^3s_1Li^+ . *Phys. Rev. A*, 21:179–187, Jan 1980. 69
- [47] A. S. Kheifets, D. V. Fursa, C. W. Hines, I. Bray, J. Colgan, and M. S. Pindzola. Spin effects in double photoionization of lithium. *Phys. Rev. A*, 81:023418, Feb 2010. 69

- [48] A. S. Kheifets. Time-dependent close coupling calculations of two-photon ionisation of lithium. private communication, 2011. 69, 71
- [49] A. Emmanouilidou, Peijie Wang, and J. M. Rost. Initial state dependence in multielectron threshold ionization of atoms. *Phys. Rev. Lett.*, 100:063002, Feb 2008. 74
- [50] G. H. Wannier. The threshold law for single ionization of atoms or ions by electrons. *Phys. Rev.*, 90:817–825, Jun 1953. 74
- [51] H. Klar and W. Schlecht. Threshold multiple ionization of atoms. energy dependence for double and triple escape. *Journal of Physics B*, 9:1699, July 1976. 74
- [52] D. A. Horner, F. Morales, T. N. Rescigno, F. Martin, and C. W. McCurdy. Two-photon double ionization of helium above and below the threshold for sequential ionization. *Phys. Rev. A*, 76:030701, Sep 2007. 74
- [53] H. Bachau. Theory of two-photon double ionization of helium at the sequential threshold. *Phys. Rev. A*, 83:033403, Mar 2011. 74
- [54] R. Pazourek, J. Feist, S. Nagele, E. Persson, B. I. Schneider, L. A. Collins, and J. Burgdörfer. Universal features in sequential and nonsequential two-photon double ionization of helium. *Phys. Rev. A*, 83:053418, May 2011. 74

Declaration

I herewith declare that I have produced this thesis without the prohibited assistance of third parties and without making use of aids other than those specified; notions taken over directly or indirectly from other sources have been identified as such. This thesis has not previously been presented in identical or similar form to any other German or foreign examination board.

The thesis work was conducted from the 21.12.2010 to the 21.12.2011 under the supervision of Priv.-Doz. Dr. Alexander Dorn at the Max Planck Institute for Nuclear Physics.

Heidelberg,